# InGrid based TPC readout

Robert Menzen

Masterarbeit in Physik
angefertigt im Physikalischen Institut

vorgelegt der
Mathematisch-Naturwissenschaftlichen Fakultät
der
Rheinischen Friedrich-Wilhelms-Universität
Bonn

September 2013

Ich versichere, dass ich diese Arbeit selbstständig verfasst und keine anderen als die angegebenen Quellen und Hilfsmittel benutzt sowie die Zitate kenntlich gemacht habe.

| | |
|---|---|
| Referent: | Prof. Dr. Klaus Desch |
| Koreferent: | Prof. Dr. Ian C. Brock |

# Contents

# Chapter 1

# Introduction

In general, particle physics deals with the composition and mutual interaction of matter in the universe. To describe known particles and forces, the Standard Model, which successfully covers weak, strong and electromagnetic forces, has been established. It is, however, not complete. For example, gravity is not included in the model. There are, among others, three big questions currently occupying the particle physics community the standard model has no answer for. The first is the question of the composition of the universe, especially what the dark matter observed by astronomy is made of. Then, there is the question why there is lots of matter, but nearly no antimatter in the known universe. And last but not least, the standard model is based on the electroweak symmetry, which does not allow the fundamental particles to be massive, predicts the Higgs field to compensate and gives mass to these particles. The standard model however fails to predict the mass of the corresponding Higgs boson - experimental evidence is needed.

Although recently a Higgs like resonance at 125 GeV has been discovered at the LHC at CERN [1],[2], this is not the best machine to have a close look at this particle, since the LHC is a hadron collider, in which composite particles, namely protons, collide. Thus, the available energy is much lower than the nominal CMS energy, and only a fraction of the proton energy will be available in a collision - this limits possible reactions, and more severe, introduces another unknown variable to the process. Besides, proton beams cannot be polarized. Another problem is the high QCD background [3], which dominates the proton-proton cross-section. The cross-section for Higgs boson and top pairs production is actually eight to eleven orders of magnitude lower than the pp cross-section - this means the trigger system has to be very sophisticated [4]. Eventually, only some of the interesting features of the Higgs boson, namely mass, parity and spin, can be measured model-independent at the LHC. Amongst other, the total width, absolute coupling and self coupling, as well as triple gauge couplings and highly precise top and W masses cannot be measured at the LHC [5].

While a $e^+$ $e^-$ accelerator suffers from high energy loss by synchrotron radiation (due to the lower mass of the electron, in the case of a circular collider) and thus needs to be a linear accelerator for high energies, it provides much cleaner reactions, since the electron has no substructure. Besides the cross section for interesting reactions is only two orders of magnitude below the total $e^+e^-$ cross-section [6]. Also electrons allow for a polarized beam, further defining the initial conditions. So the best approach for precision measurements further defining the empiric higgs boson by measuring its coupling strengths, is a linear $e^+/e^-$ collider. A promising candidate for such a collider is the International Linear Collider (ILC).

## 1.1 The International Linear Collider

The ILC, as depicted in figure 1.1, is a linear electron-positron collider with a maximal centre of mass energy of 500 GeV, which can be extended to 1 TeV in a future upgrade, while sustaining a relative

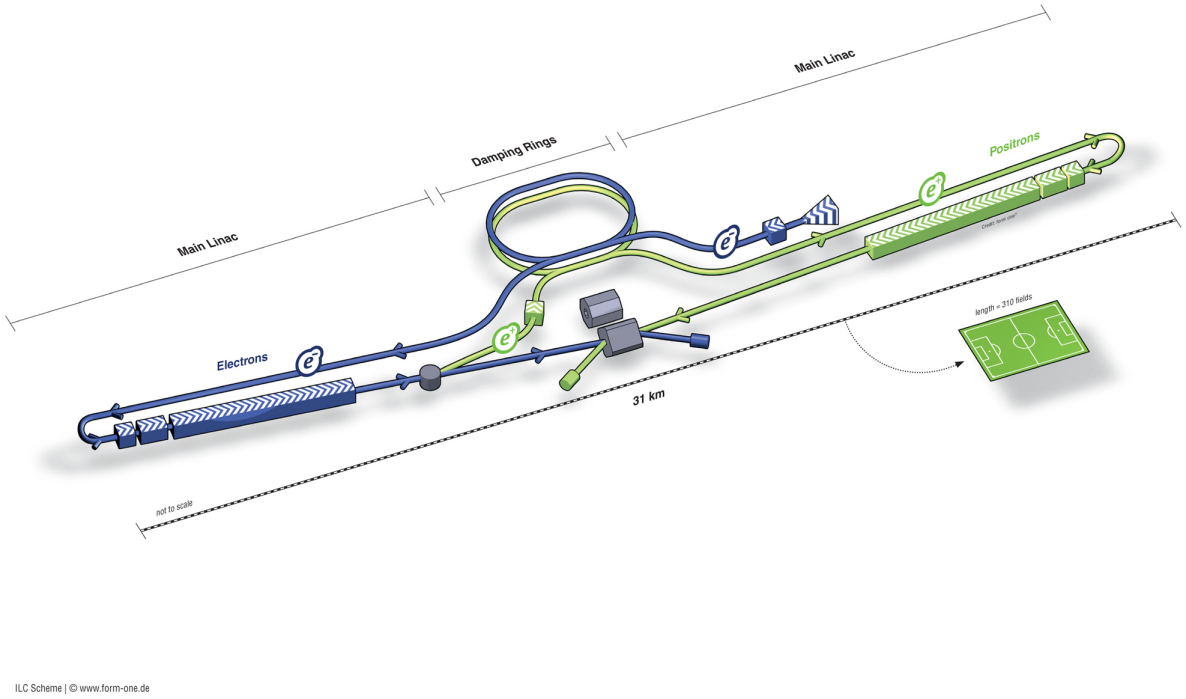


Figure 1.1: A schematic view of the International Linear Collider [9].

energy stability of ≤0.1 %. It will reach 80 % electron- and up to 60 % positron-polarization and is designed to reach a peak luminosity of $2 \times 10^{34}$ $1/(\mathrm{cm}^2\mathrm{s})$. It is 31 km long, and its major components are two linear accelerators, both 11 km long, one for positrons and one for electrons, as well as two dampening rings located in the central region. It will have two detectors arranged in a push-pull principle, namely the International Large Detector (ILD) [7], and the Silicon Detector (SiD)[8].

## 1.2 The International Large Detector

The International Large Detector, short *ILD*, is a composite detector concept with the shell structure common in modern particle physics. Closest to the interaction point, the ILD will have a vertex detector using highly precise silicon pixel sensors. It will have a radius of just a few centimeters. Going outward, it is enclosed by the Time Projection Chamber, short *TPC*, which is a gaseous tracking detector. It has a smaller single point resolution than the vertex detector, which is why it is surrounded by a layer of silicon strip detectors. It can however deliver a very high number of track points which more than compensates for the limited accuracy. As this thesis topic is TPC readout, this type of detector will be described in great detail in section 2.4. The ILD TPC is currently under development within the LCTPC collaboration, which includes more than 30 institutes spread over 3 continents. Going further away from the beam spot, the TPC is enclosed by calorimeters. First comes the electromagnetic calorimeter *ECAL*, which will consist of alternating layers of tungsten and position sensors, the latter being either silicon or scintillator based. Particles will loose energy in the dense tungsten regions such that they can be detected in the instrumented areas. The ECAL is surrounded by the hadronic calorimeter *HCAL*, which has a similar structure as the ECAL but uses steel instead of tungsten. The position sensors will either be scintillators or gaseous detectors. The outermost detector is the muon detector (as the muons traverse

the rest of the detector relatively easy), and will like the calorimeters feature a dense region, in this case made out of iron, in which the muons can interact with the detector material, resulting in showers which are registered in the active area, which will consist of either gaseous detectors or scintillators. Furthermore, the ILD features two forward detectors, the BeamCal and LumiCal, which both measure the luminosity. The magnetic field of about 4 T is supplied by a superconducting solenoid magnet which encloses the HCAL [10].

Within the scope of thesis, as a precursor for a future 100 chip module (c.f. figure 1.2), two prototype TPC modules for gas amplification and charge collection were developed and tested. Both use the Scalable Readout System and Timepix ASICs as detectors, with eight chips each. For gas-amplification, one module makes use of Gas Electron Multipliers, the other of Micromegas like InGrid structures. Fundamentals of gaseous detectors will be elaborated in chapter 2. The experimental setup for testing the prototype modules is described in chapter 4. Finally, the analysis of the data is discussed in chapter 5.

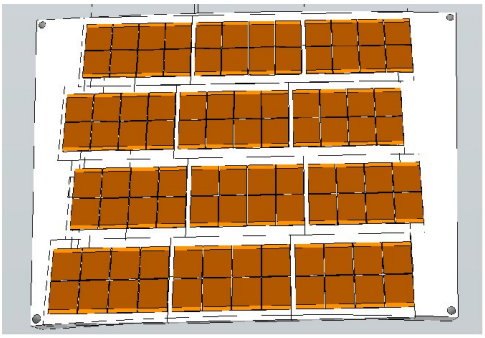

Figure 1.2: Possible chip layout on the future 96 chip module [11]

# Chapter 2

# Fundamentals of gaseous detectors

In order to explain the operating principle of a *Time Projection Chamber*, or short TPC, first some aspects of the movement of (charged) particles through gas are discussed. First, the creation of free electrons in a detector by means of ionization is discussed. Then the different types of movement inside the detector, namely drift and diffusion, are discussed.

## 2.1 Creation and transport of charge carriers in the detector gas

### 2.1.1 Ionization

Ionization is the process of either adding or removing an electron to or from an atoms hull and, thus, making it a charged ion.

**Electron capture ionization** is the attachment of an additional electron to an atoms hull. This happens when a free electron gets caught inside the atoms potential, for instance if a very electronegative atom snatches an electron from another atom. The other atom then misses an atom, making it positively charged.

**Positive ionization** can also be caused by exciting an atom beyond the ionization threshold by collision with another particle, which will transfer a portion of its energy to the atom. This can happen thermally or by collision with a energetic particle. There are two mechanisms of this kind of ionization, primary and secondary ionization.

**Primary Ionization** is the process of ejection of one or more electrons from an atom by collision with a fast particle. The energy needed to ionize an atom depends on the kind of atom, the first electron ionization energy is in the eV range. The energy required for ionization increases with every electron that was already removed, as there are less electrons present which screen off the potential of the nucleus.

**Secondary Ionization** is caused either by electrons which stem from another ionization event by a similar mechanism as above, or by creation of an intermediate excited state, which then transfers its excitation energy to another atom of another element (or a different type of molecule) which has a lower ionization threshold. Such excited states for example may be caused by a fast particle colliding with the atom as in primary ionization, with the energy transfer being insufficient to cause (primary) ionization. This is also referred to as the Penning effect [12].

### 2.1.2 Drift

Charged particles in an electrical and magnetic field are subject to the Lorentz force

$$\vec{F}_{\mathrm{L}} = q(\vec{E} + \vec{v} \times \vec{B}) \tag{2.1}$$

where the drift velocity $v_{\mathrm{Drift}}$ is limited by repeated collisions with the detector gas. Following P. Langevin [13],[14] this can be described as a friction force $\vec{F}_{\mathrm{F}} = -\frac{m\vec{v}_{\mathrm{Drift}}}{\tau}$ where $\tau$ is the average time between two collisions. It follows for the total force acting on a drifting particle:

$$\vec{F} = \vec{F}_{\mathrm{L}} + \vec{F}_{\mathrm{F}}. \tag{2.2}$$

For times much longer than $\tau$ one can assume that a steady state with $\vec{F}_{\mathrm{L}} = -\vec{F}_{\mathrm{F}}$ is reached, then the drift velocity reads as:

$$\vec{v}_{\mathrm{Drift}} = \frac{\mu}{1 + \omega^2\tau^2} \cdot \left( \vec{E} + \frac{\vec{E} \times \vec{B}}{B}\omega\tau + \frac{\left(\vec{E} \cdot \vec{B}\right)\vec{B}}{B^2}\omega^2\tau^2 \right) \tag{2.3}$$

with the cyclotron frequency $\omega = \frac{qB}{m}$ and the mobility $\mu = \frac{q\tau}{m}$. For two extreme cases, this simplifies drastically: In the case that $\vec{E}$ and $\vec{B}$ are (anti)parallel,

$$\vec{v}_{\mathrm{Drift}} = \mu\vec{E} \tag{2.4}$$

holds, if $\vec{E}$ and $\vec{B}$ are perpendicular to each other, $\vec{v}_{\mathrm{Drift}}$ reads:

$$\left|\vec{v}_{\mathrm{Drift}}\right| = \frac{\mu \left|\vec{E}\right|}{\sqrt{1 + \omega^2\tau^2}}. \tag{2.5}$$

As $\tau$ is heavily dependent on the drift gas density, and ,thus, the temperature, the above expression is also temperature dependent.

As elaborated in [15], the drift velocity of electrons yields a complex expression which can only be solved numerically, due to the strong dependence of the scattering cross section $\sigma$ on the electric field and the energy of the particle. In case of the much heavier ions, the scattering cross section is less dependant of the particle energy such that $v_{\mathrm{Drift}} \propto \vec{E}$ is valid as long as $\vec{B} = 0$ or $\vec{B} \| \vec{E}$. Another consequence of the much larger mass of the ions compared to electrons is a drift velocity which is up to three orders of magnitudes smaller.

### 2.1.3 Diffusion

Electrons and ions, which are not in a field, will exchange their energy in collisions yielding a Boltzmann distribution for their thermal energy such that

$$E_{\mathrm{T}} = \frac{3}{2}k_{\mathrm{B}}T. \tag{2.6}$$

The mean direction of movement between two encounters is randomly spread, the speed is given by

$$v_{\mathrm{Therm.}} = \sqrt{\frac{2E_{\mathrm{T}}}{m}}. \tag{2.7}$$

In an external field, the energy of a charged particle is given by the sum of kinetic and thermal energy, and according to [15] this yields

$$E = \frac{1}{2} m \left( \vec{v}_{\text{Therm.}} + \vec{v}_{\text{Drift}} \right)^2 . \tag{2.8}$$

So, not only the drift field, but also the temperature of the gas induces a movement of the charge carriers. While the movement caused by the drift field is by definition oriented along the drift field, the thermal movement is chaotic and omnidirectional. This leads to the diffusion of a point-like charge cloud to a Gaussian distributed cloud with time. According to [16] the density distribution after a time $t$ is given by:

$$N(t) = \left( 4\pi \tilde{D} t \right)^{-\frac{3}{2}} \cdot \exp\left( -\frac{r^2(t)}{4\tilde{D}t} \right) \tag{2.9}$$

with the diffusion coefficient $\tilde{D}$. The width of the charge cloud density distribution is given by $\sigma = \sqrt{2\tilde{D}t}$, which inconveniently depends on the time. If one defines the drift constant $D$ such that

$$D = \sqrt{\frac{2\tilde{D}}{v_{\text{Drift}}}} \tag{2.10}$$

and using

$$t_d = \frac{z}{v_d} \tag{2.11}$$

the width of the distribution can be much more conveniently expressed in dependence of the drift distance $z_{\text{Drift}}$ as $\sigma = D\sqrt{z_{\text{Drift}}}$.

As elaborated in [16], the diffusion coefficient depends on the thermal energy of the diffusing particles. This can be shown by having a closer look on the dependence of $\tilde{D}$ on the mean free path $\lambda = \tau v_{\text{total}}$ which reads:

$$\tilde{D} = \frac{\lambda^2}{3\tau} = \frac{1}{3}\tau v_{\text{total}}^2 = \frac{2}{3} E_{\text{T}} \frac{\tau}{m}. \tag{2.12}$$

From the above equation one can also deduce that an electric field leads to non-isotropic diffusion constants. This affects the $xy$ and $z$ widths of a charge cloud which now read:

$$\sigma_{\text{xy}} = D_{\text{T}} \sqrt{z} \tag{2.13}$$

$$\sigma_{\text{z}} = D_{\text{L}} \sqrt{z}. \tag{2.14}$$

To reduce the diffusion, the most obvious choice is using a slow gas and cooling the detector, which reduces both $D_{\text{T}}$ and $D_{\text{L}}$. Another way to reduce $D_{\text{T}}$ is the application of a magnetic field parallel to the drift field, which forces the electrons on a more stable helix shaped path, which reduces diffusion according to

$$\frac{D_T(B)}{D_T(0)} = \frac{1}{C + \omega^2 \tau^2} \tag{2.15}$$

where $C$ is a parameter depending on the gas and the magnetic field. For magnetic fields below 0.2 T it approaches 1 ([16],[17]).

## 2.2 Gas amplification structures

As there is currently no technology available which can directly detect single electrons in a gas volume, the electrons have to be multiplied prior to detection. This is done by accelerating the electrons by means

of a high electric field ($\approx 100\,\mathrm{kV\,cm^{-1}}$) such that their kinetic energy is sufficient to cause secondary ionization. The newly freed electrons are then accelerated, until their energy is sufficient for ionization as well, this way, eventually, an electron avalanche develops. The number of electrons $N(r)$ created by $N_0$ electrons on the path of length d$r$ is given by

$$\mathrm{d}N(r) = \alpha(r) N_0 \mathrm{d}r \tag{2.16}$$

with the 1st Townsend coefficient $\alpha = 1/\lambda$, where $\lambda$ is the mean free path between two collisions. On a non-infinitesimal path $r_1 \rightarrow r_2$ this becomes

$$N = N_0 \exp\left(\int_{r_1}^{r_2} \alpha(r)\mathrm{d}r\right) = N_0 \bar{G} \tag{2.17}$$

with the mean gas gain $\bar{G}$. This process is called gas amplification, and yields an electron cloud which can be detected by standard readout electronics. The gas gain for a given gas amplification structure is not a fixed number but a distribution since gas amplification is a statistical process. For analytic purposes, and in the case of an inhomogeneous magnetic field, the above dependency can be described by a Pólya-distribution [12]:

$$P(G) = \frac{1}{\bar{G}} \frac{(\Theta+1)^{\Theta+1}}{\Gamma(\Theta+1)} \left(\frac{G}{\bar{G}}\right)^{\Theta} \cdot \exp\left(-(\Theta+1)\frac{G}{\bar{G}}\right) \tag{2.18}$$

where $\Theta = \frac{(\bar{G}-\sigma^2)}{\sigma^2}$ is a parameter depending on the width $\sigma$. The gas gain depends on the field strength in the gas amplification structure and the ionization energy, as well as the mean free path length in the gas. The latter depends on the density of the gas, which adds pressure and temperature dependencies to the equation. The temperature dependence of the gas gain in a triple GEM stack (c.f. section 2.2.1) was studied in [18] for helium, argon and krypton. For helium, the gas gain is largely temperature independent in the range of 120 to 300 K, while for argon and krypton the gas gain decreases by a factor of 2-3 in this range. It is theorized that this drop is caused by associative ionization.

The accuracy of such a detector is dependent on the granularity of both the gas amplification structure and the readout electronics.

The first gas amplification structures were simple wires. In vicinity of these wires, the electric field is large enough to cause gas amplification. A current is induced on the wires, leading to a detectable signal. If a detector consists of multiple wires, it is called a *Multi Wire Proportional Chamber* or MWPC. For wires, the granularity is defined (and limited) by the distance of the wires. The impact position in the direction parallel to the wires is calculated from the time it took the signal to propagate from the impact position to the end of the wire, which is less accurate than in the direction perpendicular to the wires. In the case of the MWPC this is improved by the addition of cathode strips behind the wires, which are used for charge collection and readout.

Since the first days of gas amplification structures, different approaches have been followed to increase the readout accuracy. A promising path are the *Micro Pattern Gaseous Detectors*, or short MPGDs. These use some kind of microscopic grid-like structure for gas amplification, and strips, pads or pixel-chips for readout. As in this thesis pixel chips were used for readout, other readout designs are not being discussed. All these structures basically consist of one or more thin perforated layers, with the hole diameters in the order of several µm. Then an electric field is applied either between both sides of the foil, or between the foil and the readout plane. In either case, a high electric field in the order of 100 kV per centimetre is present in (and/or underneath) the hole, and an avalanche then develops within

the micro pattern gas amplification structure.

### 2.2.1 Gas Electron Multiplier

A (standard CERN) Gas Electron Multiplier, short *GEM* is an insulating foil made out of 50 µm thick Kapton. This foil is covered with 3 µm of copper on both sides. It has double conical holes in a hexagonal pattern with a pitch of 140 µm and a diameter of 50 µm in the hole center. The electric field is applied between the copper coating on both sides, yielding a field strength of about 100 kV cm$^{-1}$ in the holes, yielding a gain of about 100 to 10000. If one, however, uses a stack of three GEMs, the gas gain multiplies, and can be in the order of $10^3 - 10^5$, which is sufficient for detection. Usually $G \approx 10^3$ is enough, $G \approx 10^5$ is only needed for pixellated readout. A GEM stack also reduces the drift of ions back into the detector volume due to the external electric field, compared to a single GEM, as ions are caught on the other GEMs. The behaviour of electrons and ions within a GEM stack was studied in [19],[20],[21], and GEMs are discussed in great detail in [15], [22]. A microsopic image of a GEM foil is shown in figure 2.1a.

### 2.2.2 Micromegas

Micromegas are made of a mesh structure, their holes have a pitch of about 50 µm, located 50-100 µm above the readout plane. Here, the electric field is applied between the micro-mesh and the readout plane, such that amplification does not take place within the holes of the micro-mesh, but within the amplification gap between grid and chip. A feature of this detector is that both ions and electrons contribute to the signal, since the ion signal is very short due to the small amplification gap (the electron signal is still shorter of course). The gas gain in a Micromegas is usually in the order of $10^3$, however a gas gain of about $3 \cdot 10^5$ was realized. [15],[23], [24]

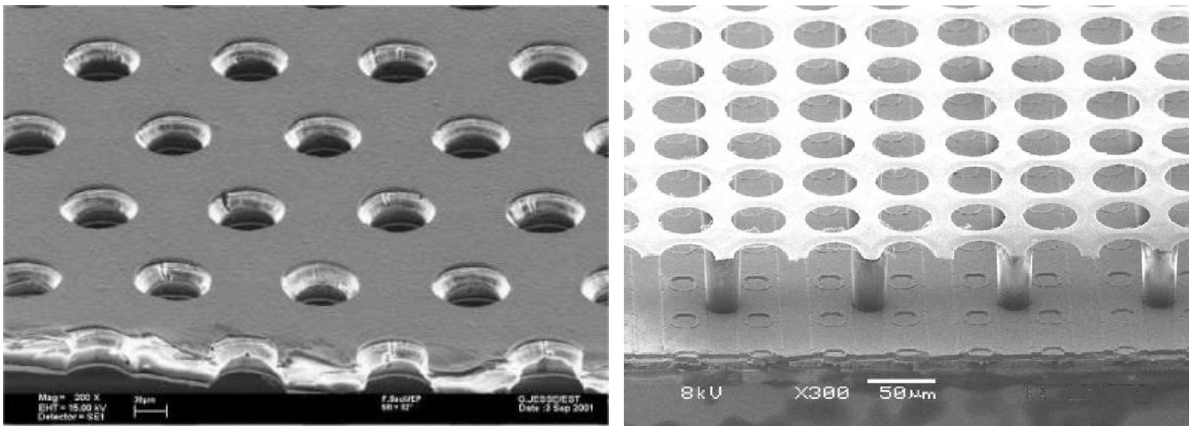


(a) Microscopic image of a GEM [25]

(b) Microscopic image of a Micromegas (InGrid)[26]

Figure 2.1: Images of the two types of MPGD used in this thesis. [25],[26]

## 2.3 Pixellated Readout

### 2.3.1 The Timepix chip

The Timepix chip is a $256 \times 256$ pixel chip with an active area of $(1.4\,\mathrm{cm})^2$, based on the Medipix2 chip [27]. The pixel size is $55\,\mu\mathrm{m} \times 55\,\mu\mathrm{m}$. Expanding the Medipix2 chips features, the Timepix is able to measure not only charge but also arrival time, though not both at the same time in one pixel. For coincident measurement of both quantities, a chequerboard pattern with pixels in alternating modes can be used in a setup with GEMs.

The analog part of the pixel consists of a pre-amplifier and a discriminator, and is directly connected to the bump bond pad. Charge, collected in a pixel, is integrated, pre-amplified and compared to a threshold value. If the charge value is above the threshold, the discriminator creates a pulse which length depends on the time the preamplifier output was over threshold. This signal is then called a hit.

The digital part houses the synchronization logic, two multiplexers and a 14 bit shift register. It defines the pixel operation mode, which can be externally set, and synchronizes the shutter and hit signals with an external reference clock. It also stops the counter if the number of counts reaches the maximal value which is 11 810 counts.

In a measurement in time over threshold (ToT) mode, the counter is incremented with every reference clock cycle as long as the discriminator output is at the high level.

In the Time of Arrival (ToA) mode, the counter keeps incrementing with every clock cycle while the discriminator and shutter are high. Thus, converting the hit information to a time measurement. The quantization error can reach two clock cycles. [28]

For calibration purposes, there is the option of directly applying charge pulses to the pixels. If one injects pulses of different height into the chip, from the height of the input pulse and the measured chip response in a calibration can be derived (see section 5.5.2).

A bare Timepix chip can be placed beneath a triple GEM stack or a Micromegas for charge collection. An alternate approach is the realization of a Micromegas directly on a Timepix chip by means of post processing. This is discussed in section 2.3.2.

### 2.3.2 InGrid

InGrid is short for *Integrated Grid*. InGrid devices are micro patterned gas amplification structures directly applied on top of a Timepix chip by photo-lithographic processing (as shown in a large magnification in figure 2.1b). This allows for good alignment of pixels and grid holes, and good uniformity of the grid to pixel distance leading to good gain homogeneity, both greatly improves the accuracy and allows for precise 3D track measurements. InGrids have a higher resolution compared to other Timepix based readout concepts, as the resolution is determined by the $50\,\mu\mathrm{m}$ hole pitch. Additionally, due to the small distance between grid and chip, it can be assumed each electron created underneath one hole will hit the underlying pixel, without any electrons spreading to neighbouring pixels. Another advantage is that in the case of InGrids both gas amplification and readout are integrated into a single device [29].

Both the grid holes and the pillars supporting the grid have a diameter of $30\,\mu\mathrm{m}$. This means the pillars can be placed between the holes, this way inactive regions are avoided [30]. The pillars are $50\,\mu\mathrm{m}$ high, defining the width of the amplification gap [26].

The gas amplification of an InGrid can reach the order of $10^4$.

### 2.3.3 Spark Protection

Sparks are electric discharges occurring in various types of gaseous detectors. Under the effect of a high electric field they can be caused by a highly ionizing particle and take the form of an conductive plasma cloud connecting anode and cathode. These sparks can cause considerable damage to a Timepix chip, thus, efforts have been made to protect the chip surface from such discharges. It was established that a layer of a−SiH or SiRN of a few micrometers thickness protects the chip from discharges without impairing its normal function [31].

## 2.4 Time Projection Chambers

A Time Projection Chamber (TPC) is a gas filled volume in a capacitor, with readout electronics on the anode side. The volume is usually a cylinder placed around the beam pipe, with the end-caps being the capacitor plates. In collider TPCs, the cathode is usually in the middle of the TPC, using both end-caps as anodes. This reduces the drift distance by one half. The electric field is applied between cathode and anode, field strips are added to increase field homogeneity. If a fast particle passes through the TPC, it ionizes the detector gas, leaving a trail of ions and electrons. Due to the electric field, the ions drift to the cathode while the electrons drift to the anode. One chooses to place the readout on the anode rather than the cathode because gas amplification of positive ions is not an option, and the electrons drift much faster than the ions due to their lower mass and thus higher mobility. A magnetic field is added perpendicular to the readout plane such that charged particles have a curved trajectory, making momentum measurements and charge determination possible. Another advantageous effect of the magnetic field is a reduction of electron diffusion (c.f. section 2.1.3). As electrons created further away from the anode also arrive later, the readout at the anode can measure all the information needed for full 3D track reconstruction - the track of the primary particle is projected time-encoded on the readout plane, hence the name of this type of detector. The track of the primary particle is then characterized by four parameters, which are illustrated in figure 2.2a, and the track curvature. $d_0$ is the minimal distance of the track projection in the $xy$-plane to the origin, and $\phi$ the corresponding angle. $z_0$ is the distance from track and $xy$-projection at the point closest to the origin and $\lambda$ is the angle in the track projection vs $z$ plane. The electric field in the drift region is relatively weak and the electrons have to be multiplied

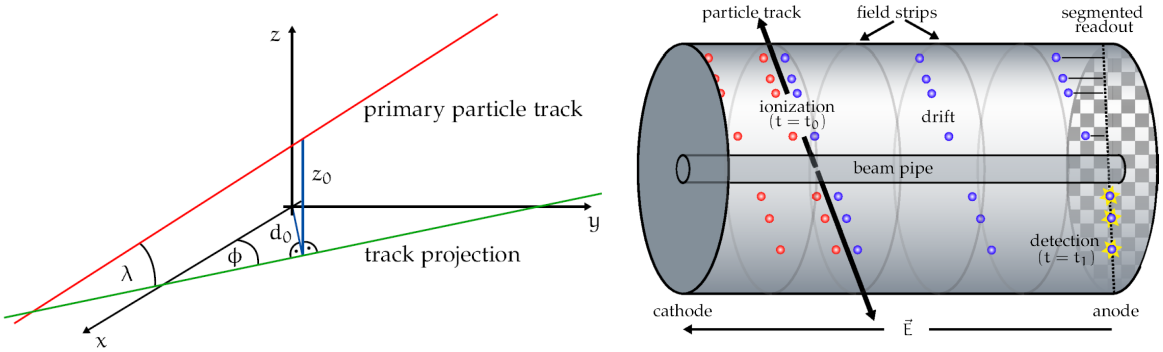


(a) Definition of the four track parameters.

(b) Schematic of a TPC. Two particles originating from the interaction point leave trails of ions and electrons, which drift towards the end-caps.

Figure 2.2: TPC and track description. [15]

in vicinity of the readout. This is done by one of the gas amplification structures discussed in section 2.2. A schematic view of a TPC is shown in figure 2.2b.

Due to unavoidable diffusion on the electrons path from track to readout plane, the single point resolution of a TPC is not as good as in the case of modern silicon detectors, its greatest advantage is the huge number of track points recorded due to the continuous active gas volume. It is also relatively cheap to cover large volumes with a TPC tracker, hence TPCs reach volumes of several cubic meters.

# Chapter 3

# Basics of thermodynamics

As discussed in section 2.1.3, the temperature of the gas influences diffusion and gas amplification properties. Thus it is important to keep the detector at a constant temperature. Consequently, it is necessary to understand the heat production and distribution in the detector. The three major mechanisms of heat transport will be summarized from [32].

## 3.1 Thermal radiation

Thermal radiation is electromagnetic radiation caused by different effects within a heated material. A major contribution is temperature induced acceleration of electrons within a material, this can be free electrons in a plasma or conduction electrons within a solid. As with higher temperature the thermal velocity of these charge carriers rises, the collision probability increases and ,thus, the rate of acceleration (or deceleration), leading to the emission of EM-radiation. This also explains why thermal radiation is material independent, and shows a continuous spectrum as the velocities and thus the associated acceleration/deceleration upon a collision are statistically distributed. Another cause for thermal radiation are lattice vibrations, which also increase with rising temperature. The emitted power $P$ is in both cases related to the temperature $T$ according to the Stefan–Boltzmann law:

$$P = \sigma \cdot A \cdot T^4, \tag{3.1}$$

with the surface-area $A$ and the Stefan–Boltzmann constant $\sigma$. According to Kirchhoff's law:

$$\alpha_\lambda = \varepsilon_\lambda \tag{3.2}$$

the emissivity $\varepsilon_\lambda$ of a body for a given wavelength is the same as its absorptivity $\alpha_\lambda$ for that wavelength. This means good absorbers are good emitters, and vice versa. While thermal radiation does not depend on the material, emission and absorption of thermal radiation are largely dependent on the surface consistency. Reflective white surfaces are the least effective absorbers/emitters, while matte black surfaces are the most effective ones.

## 3.2 Convection

Convection appears in volumes of fluids or gases, which are non-uniformly heated. Convection is the only type of heat transport, in which not only energy, but also mass is transferred. The particles in the heated area gain thermal energy, resulting in a statistically oriented movement. Due to the resulting collisions the pressure rises and, consequently, the particles move further away from each other, also into the non-heated regions. Here they again collide with particles of the previously non-heated volume, and in result the cooler volume is heated as well - heat transfer has taken place, and for relatively

weak heating a linear temperature gradient will develop. If, however, a certain threshold, depending on the materials viscosity, is crossed, non linear movement of the particles is the result. In this case current tubes develop, and the particles move on cylindrical paths. This has to be avoided in gaseous detectors, as gas currents inside a TPC would distort the recorded tracks, due to changed drift and diffusion properties. This effect is also to be avoided in cooling systems, as laminar currents in the coolant dissipate heat from the cooled part better than turbulent currents. This is the case as the current tubes developing in the latter case rather store the heat as opposed to moving it away.

## 3.3 Thermal conduction

Thermal conduction is the heat transfer caused by coupling between neighbouring atoms, heat is transferred in the form of vibrational energy from an atom to it's neighbours. Especially in metals, electrons also contribute to thermal conduction due to collisions with nuclei and other electrons. This is why the thermal conductivity $\lambda$ largely depends on the electric conductivity $\sigma$ of a material, as described by the Wiedemann-Franz law:

$$\frac{\lambda}{\sigma} = \frac{\pi^2 k^2}{3e^2} \tag{3.3}$$

with the Boltzmann constant $k$ and the elementary charge $e$. Thermal conduction is more effective in solids than in liquids, as in the latter case the atom-to-atom coupling is weaker. In gases however thermal conduction occurs at about the same rate as in solids. While the atom-to-atom coupling, like in liquids, is comparably weak, the density is much lower, to. Thus a smaller amount of heat can bring a larger volume to the same temperature, as compared to a solid body.

For a homogeneous cuboid with cross-section $a$ and length $l$ which is heated on one side to $T = T_1$, and cooled on the opposing side to $T = T_2$, as done in section 4.3.2, a temperature gradient develops depending on $l$ and the temperature difference. Under the assumption of negligible heat loss through the remaining sides of the cuboid, the heat flow can be described as:

$$\frac{\mathrm{d}Q}{\mathrm{d}t} = -\lambda \cdot a \cdot \frac{\mathrm{d}T}{\mathrm{d}x}. \tag{3.4}$$

Still assuming negligible heat loss through the sides, one can obtain an expression for $T(x)$ by integration, which yields

$$T(x) = -\frac{\mathrm{d}Q/\mathrm{d}t}{\lambda \cdot a} + T_1. \tag{3.5}$$

For the realistic case of a non-homogeneous material and non-negligible heat loss through the sides this expression is no longer valid, and the problem is solvable only numerically.

## 3.4 Thermal resistance

The absolute thermal resistance, $R_T$, is a measure for the temperature difference needed to transfer heat in a given material. There are many parallels to the electric resistor, which allow for the use of Ohm's law and Kirchhoff's circuit laws when considering thermodynamic problems. Here, the temperature difference $\Delta T$ corresponds to the voltage, and the rate of heat flow $\dot{Q}$ the the current. Furthermore, the thermal conductance $\lambda$ corresponds to the electric conductance. Thus, just like for an electric resistor,

the thermal resistance can be computed according to

$$R_T = \frac{d}{\lambda A}. \tag{3.6}$$

Another important feature of this analogy is, that in order to calculate the total thermal resistance of a stack of objects in the direction of the surface normal, the thermal resistances of the individual parts can simply be added. They behave like serial resistors. [33],[34]

# Chapter 4

# Experimental Setup

For our test of an InGrid and a GEM based eight-chip Timepix board for TPC readout, we used the infrastructure available at DESY (*Deutsches Elektronen SYnchrotron*), especially the Large Prototype (LP) which is described in section 4.2. The LP TPC hosted our module carrying the readout boards as described in section 4.3. The module was finally read-out using the Scalable Readout System, short SRS, described in section 4.4.

## 4.1 DESY II

DESY II is a $e^+/e^-$ synchrotron at DESY in Hamburg. Its circumference is 292.8 m and the beam can reach an ejection energy of 6 GeV. It feeds electrons and positrons to the facilities DORIS and PETRA, as well as three testbeam stands. For the test of our modules the T24/1 testbeam area was used, which is one of the three serviced testbeam stands. The electron beam available at T24/1 is decoupled from DESY II by creation of a photon beam by bremsstrahlung at a carbon fibre in the DESY II synchrotron. The photons are converted to electrons and positrons via pair production in a metal plate. Electrons and positrons are then separated by a dipole magnet, and a collimator selects the electron beam. This is schematically shown in figure 4.1. Since bremsstrahlung has an $\frac{1}{E}$ energy dependence, electrons of diverse energies are available after pair production (which has a quite flat distribution). Thus, one can select electrons of a given momentum in the range of 1 to 6 GeV by tuning the magnetic field.

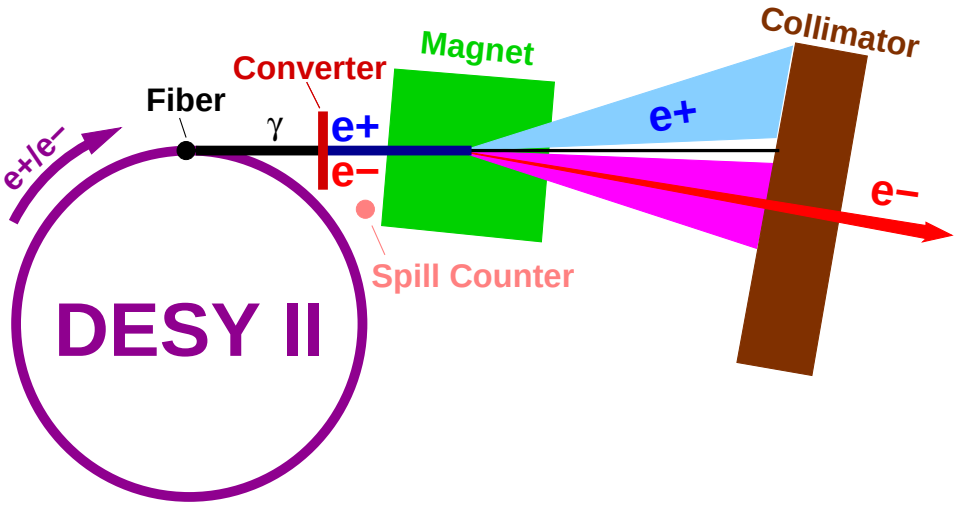


Figure 4.1: Schematic of the electron generation at the DESY II testbeam. [35]

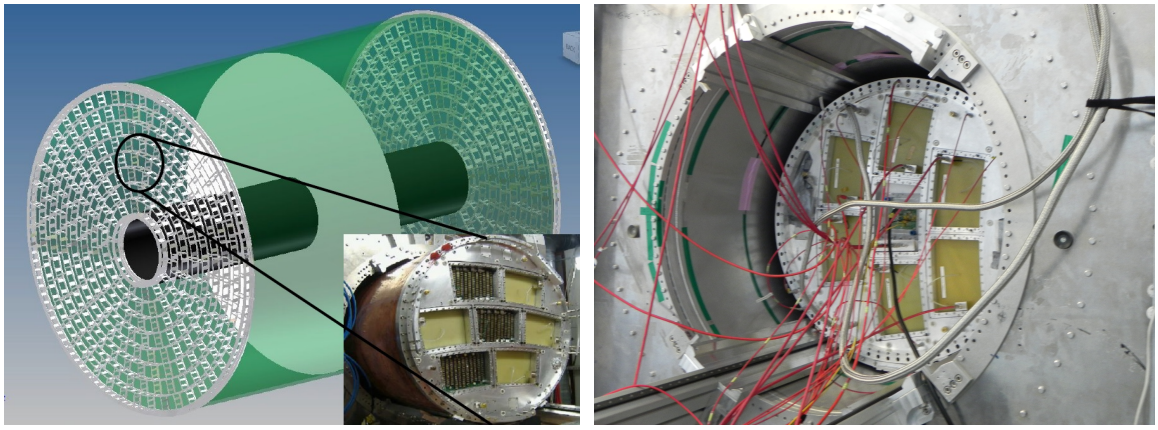

(a) LP as a cut-out of the ILD tpc [37]

(b) InGrid module installed at the LP

Figure 4.2: a): A schematic view of the LP endplate, displaying the portion of the ILD tpc it represents. b): A photograph of the InGrid Module installed in the center of the LP. The whole tpc can be rotated and moved in and out.

## 4.2 The LCTPC Large Prototype

The LCTPC Large Prototype (LP) is a TPC developed to test and compare various readout and gas amplification techniques in order to choose the most suitable technology for the future ILD TPC. The LP is designed for modular readout which can be easily exchanged. The setup is displayed in figure 4.2. The LP has room for up to seven modules, allowing for simultaneous testing of different readout techniques. The TPC has a diameter of 75 cm and is 60 cm long [36]. The LP and it's field cage are located within a persistent current magnet. The LP can be rotated and moved in and out of the magnet. The whole setup rests on a movable lifting stage.

The field cage is made of two plates at the cylinder end-caps, on the anode side with openings for modules, and two layers of field forming copper electrode rings along the cylinder wall. These field forming components are supported by a honeycomb-like support structure, which allows both mechanical stability and a low material budget [38].

The magnet is a super-conductive magnet which can create a magnetic field of up to 1.2 T. It has an active length of 100 cm and an inner radius of 86 cm. In 2007 a highly precise field map was measured [39].

## 4.3 Large Prototype Modules

In the scope of this thesis, two modules, one using InGrids, the other using GEMs for gas amplification were designed for operation at the LCTPC Large Prototype at DESY, Hamburg. They are be described in full detail in the following sections.

### 4.3.1 Design goals

Apart from the outer dimensions of the module, defined by the LP/ILD design, there were several design goals which were pursued during development of the LP modules.


(a) Longitudinal field component

(b) Transverse field component

Figure 4.3: Left: The drift field in z direction. Right: inhomogenities of the field in x direction. [40]

**Cooling** In order to dissipate the heat produced by the Timepix chips, the modules were designed with a water cooling system detailed in section 4.3.2.

**Board exchangeability** Both modules were designed in such a way, that the electronic parts can be removed while the module is installed in the TPC, in case a malfunction occurs. This was realized by constructing the module such that the cooling unit, which holds all the electronics, can be easily removed from the module.

**Field stability (InGrid)** To minimize field distortions at the edges of the board, the anode was designed such that the edges coincide with the edges of the grids. Simulations of the drift field in this case are shown in figure 4.3. As one can see, there are only minimal distortions at the anode edges.

### 4.3.2 Cooling

A Timepix chip consumes about 1 W of power (13.5 µW per pixel [28], with $256^2$ pixels yields 0.88 W), which is eventually emitted as heat. For a large detector, module cooling would be required to keep the chips at a well defined temperature, and to avoid convection induced distortions in the detector gas. First tests have been performed with the 8-Chip modules prepared and discussed in this thesis.

To understand the Timepix chip as a heat source, some basic experiments, which will be described in the following sections, have been conducted.

#### Emulation of the Timepix heat production

As a first experiment, to estimate the temperature, a Timepix chip under full load would achieve, a Timepix chip was thermally emulated by a 1 Ω power resistor (see Fig. 4.4b). With an applied voltage of 1 V, a current of 1 A flows, such that 1 W of power is dissipated in the resistor. This way it emits a comparable amount of heat as a Timepix chip. Such a resistor was attached to a 20 cm × 3 cm × 0.1 cm copper strip with thermal glue and packed in expanded polystyrene for isolation (c.f. figure 4.4a), such that most of the heat is drained by the copper strip. This way one can assume that the

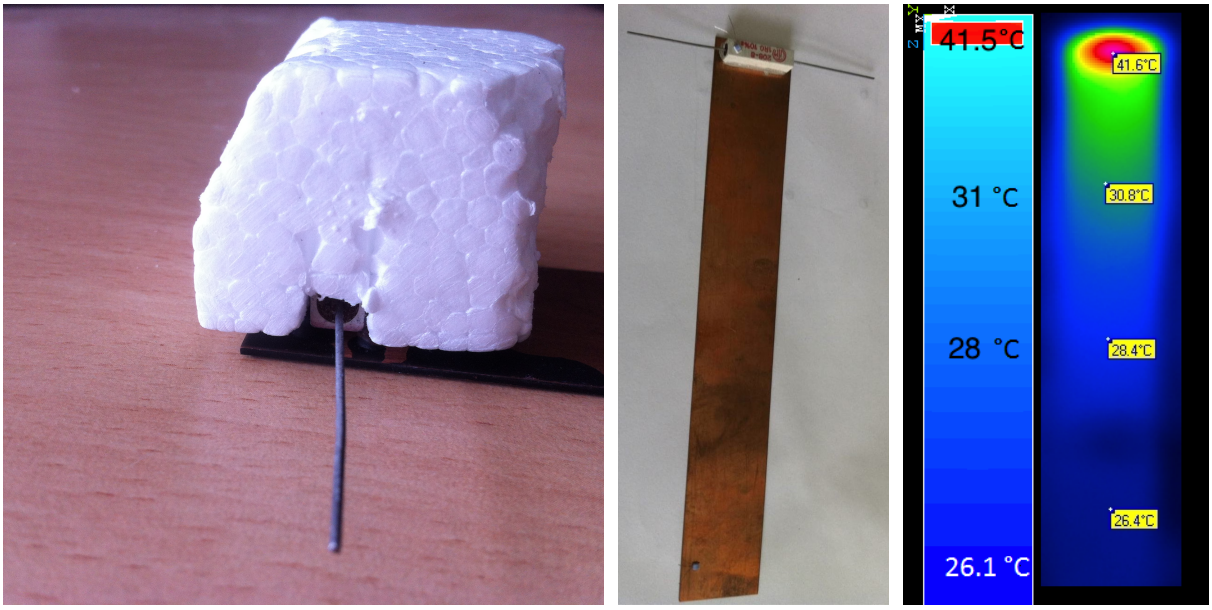


(a) Thermal isolation (b) Setup (c) Results

Figure 4.4: a): Resistor packed in expanded polystyrene b): Setup: A 1 Ω resistor was glued onto a copper strip as radiator, and then heated with 1 W of power. The temperature was measured using a liquid nitrogen cooled infra-red camera. For this, the whole setup was coloured black to improve emittance behaviour. c): Comparison of simulated and measured data. The left hand side plot shows simulated data, the right hand side measured data. The agreement is well within error margins, which in both cases is about 0.5 °C

temperature at the rear side of the copper strip closely matches the resistors core temperature. It cannot be measured directly due to the porous surface of the resistor case, as the temperature was measured with a thermographic camera, which has a limited accuracy for such surfaces. A reflective copper surface would pose an even bigger problem, as heat from other sources would then be reflected back into the camera. To circumvent this, the copper was coloured in matt black.

As a result of heating the resistor, a temperature gradient emerged on the copper strip, as discussed in section 3.3.

The cooling of the resistor due to the copper strip was also studied, the model with copper strip was compared to a free resistor. Here one would expect a higher temperature.

As a precursor to future full module simulations, both models were also simulated with the ANSYS software package. ANSYS allows one to resemble any combination of geometrical shapes, and to assign different physical properties like density, conductivity, resistivity etc. to them. It is also possible to assign different mesh types to the different bodies, for example there are different types available for different crystal lattices, or to describe fluids and gasses. Finally, ANSYS allows one to subject the created structures to a large variety of physical conditions. In the simulation, the resistor was treated as a cylindrical metal body in a cuboid ceramic casing. In case of the cooled resistor, the glue was represented by a thin cuboid between the resistor and the copper strip. The different parts were then glued together, which is a function that combines the surfaces of affected bodies, while maintaining their physical properties. In both cases, a voltage of 1 V was applied to the resistor, which resulted in the heating of the resistor, just like in reality. All areas not in contact with another body were subject to convection. Heat radiation was neglected, which is justified by the agreement of simulation and

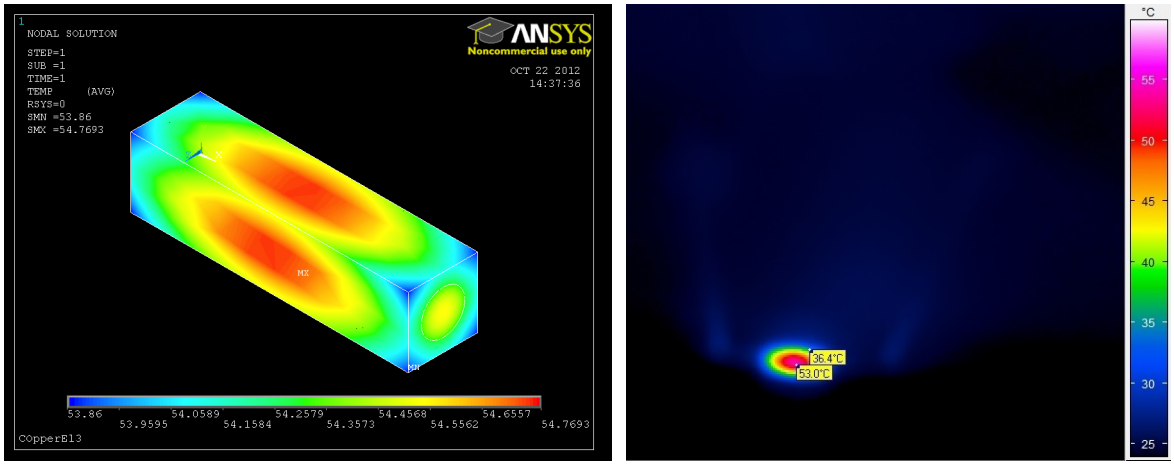


(a) Free resistor (b) Free resistor

Figure 4.5: Heated resistor. a): ANSYS simulation. b): Thermographic image.

| | T in °C, free | T in °C, cooled |
|---|---|---|
| Measured | 53.0 ± 0.5 | 41.6 ± 0.5 |
| Simulated | 54.7 ± 0.5 | 41.5 ± 0.5 |

Table 4.1: Measured and simulated temperatures for a heated resistor, cooled and not-cooled. The cooling was done by attachment of a copper radiator.

measurement.

As shown in figures 4.4c and 4.5 simulation and experiment are in good agreement. Simulation and measurement results are summarized in table 4.1. The agreement between simulation and experiment is within error margins, and the temperature is about 12 °C higher than in the case of a cooled resistor. This successful simulation of the rather simple resistor-copper system paves the way for possible more complex simulations in a future work, and gives an estimate for the temperature rise inside a detector module due to the heat production of a Timepix chip.

### Thermal conductivity of vias

The effective heating of a Timepix chip is largely dependent on two factors - the power consumption, which is fixed by the chip design, and the cooling provided by the carrier board. The latter depends mostly on the carrier boards thermal conductivity. The higher it is, the better the produced heat can be dissipated by the aluminium cooling structure the carrier board rests upon. The conductivity of the PCB material itself is very low, about $\lambda_{\mathrm{PCB}} = 0.3\,\mathrm{W\,m^{-1}\,K^{-1}}$ [41] for FR4, as it has to be manufactured out of insulating materials (usually laminates and glass fibres). Thus it is assumed that vias, electrical connections between different layers in an electronic circuit made out of copper ($\lambda_{\mathrm{Cu}} \approx 300\,\mathrm{W\,m^{-1}\,K^{-1}}$) tubes, make a sizeable contribution to the PCBs overall thermal conductivity. As vias usually cover only a small percentage of a PCB, the influence on the overall thermal conductance through the PCB is a priori unknown. One via has a diameter of 300 µm and has a copper layer thickness of about 20 µm [41]. The hole is filled with air, which has a thermal conductivity of $\lambda_{\mathrm{air}} = 0.0262\,\mathrm{W\,m^{-1}\,K^{-1}}$ [42].

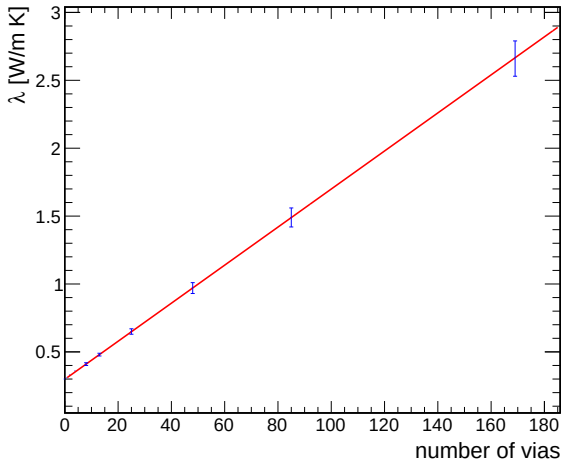


Figure 4.6: Estimated change in thermal conductivity in a FR4 PCB in dependence of the number of vias.

Thus, the total thermal conductivity of a via can be calculated by area-weighted averaging:

$$\lambda_{\text{via}} = \frac{\lambda_{\text{Cu}} \cdot A_{\text{Cu}} + \lambda_{\text{air}} \cdot A_{\text{air}}}{A_{\text{Cu}} + A_{\text{air}}} = (39 \pm 2)\ \text{W m}^{-1}\ \text{K}^{-1} \tag{4.1}$$

where $A_{\text{Cu}} = \pi \cdot (300\,\mu\text{m})^2 - \pi \cdot (280\,\mu\text{m})^2 = 9111\,\mu\text{m}^2$ and $A_{\text{air}} = \pi \cdot (140\,\mu\text{m})^2 = 61\,575\,\mu\text{m}^2$ are the surface areas those materials make up in a via. Using the above equation, one can also compute the gain in thermal conductivity per via added to a PCB of a given area, for example the area of a Timepix chip. For this, the total thermal conductivities of PCBs of fixed areas with $n$ vias are computed. One expects a linear dependency, since the total thermal conductivity is calculated by weighted averaging. As shown in figure 4.6 this is the case. The dependency of the thermal conductance of a PCB piece of fixed size on the number of vias added then follows:

$$\lambda(n_{\text{vias}}) = m \cdot n_{\text{vias}} + \lambda_{\text{PCB}}. \tag{4.2}$$

The slope is calculated to $m = (0.0140 \pm 0.0005)\ \text{W m}^{-1}\ \text{K}^{-1}$. This is the gain, in terms of thermal conductivity, per via on a PCB of the area of a Timepix chip.

With a setup similar to the one described in the previous section, namely a resistor as heat source and a copper strip as radiator, this influence was also studied experimentally. For this, several square PCB pieces with approximately the area of a Timepix chip, and with different via densities, were used. Numbers ranged from zero to 169 vias. The PCB pieces had four layers and solder resist was applied on both sides. The PCB pieces were glued on copper strips of 20 cm × 3 cm × 0.1 cm with thermal glue. A 1 Ω power resistor was glued on top of the PCB. Pictures of the setup are shown in figure 4.7. A voltage of 1 V was applied to the resistor, such that it consumes the same amount of power as a Timepix chip. Thus, it was heated, and the heat flux through the PCB was observed by measuring the temperature on the rear side of the copper strip.

To take into account the non-constant room temperature, the data was offset corrected by the room temperature according to

$$T_{Cu,Korr} = T_{Cu} - T_{Room}. \tag{4.3}$$

The room temperature was measured for each datapoint individually.

Judging from the estimation presented in figure 4.6 one would expect a linear rise in the copper

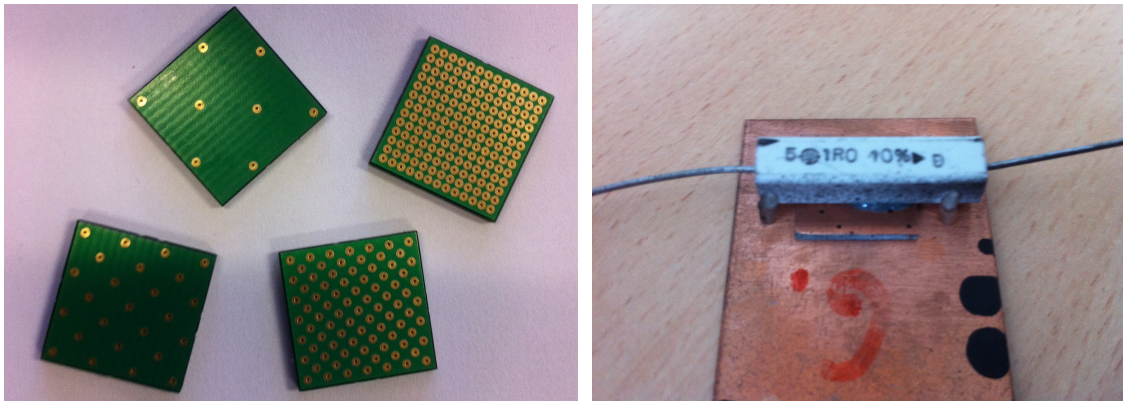

(a) (b)

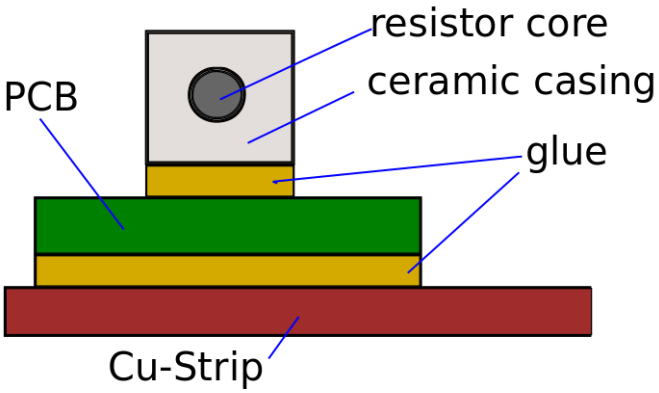


(c)

Figure 4.7: a): PCB pieces with different via densities. b): Setup for the via heat conductivity experiment. The PCB is glued onto a copper strip, and a Resistor is then glued onto the PCB piece. c): Schematic of the setup.

strip temperature with the addition of more vias to the PCB. As can be seen in figure 4.8 however, more than about 15 vias per $2\,\mathrm{cm}^2$ have only negligible effect. This can be explained by re-considering the experimental setup. The thermal glue used to glue the resistor, PCB and copper strip together has a rather low thermal conductivity compared to the thermal conductivity of a via, in the order of magnitude of $1\,\mathrm{W\,m^{-1}\,K^{-1}}$. It is present, however, only in a very thin layer. To estimate the thermal resistance of the individual slices of the setup, shown in figure 4.7, the dimensions of each slice are estimated. The thermal resistance is calculated according to equation 3.6 for each slice individually. As shown in table 4.2, the PCB has the largest thermal resistance, even with maximal via density. However, for rising via count on the PCB, the glue slices become more and more important, since the PCBs thermal resistance is reduced with each via added. Thus, as as the PCBs thermal resistance approaches the thermal resistance of the glued joints, the addition of more vias has only diminishing effects. Therefore, it is not surprising, that the temperature of the copper strip no longer increases notably once the PCB piece surpassed the thermal conductivity of the thermal glue by addition of more vias. This was studied further by computing the thermal resistance of the PCB in dependence of the number of vias. This was done with both theoretical and measured data. Since the latter only yields the thermal resistance of the entire setup, the theoretical values were offset to correct for this according to table 4.2. Additionally, further uncertainties are added, as

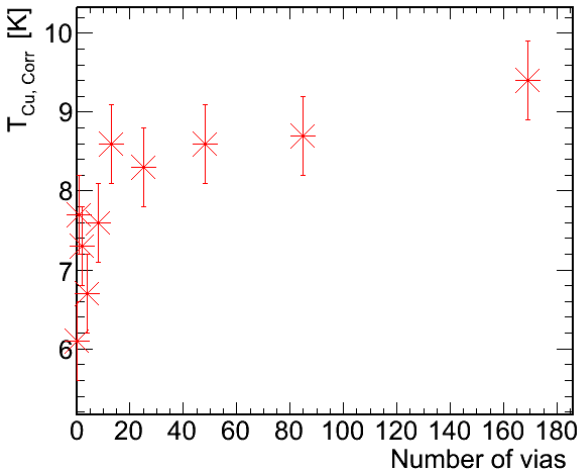


Figure 4.8: Measured thermal flux through the via plane.

| | $\lambda$ [W m$^{-1}$ K$^{-1}$] | relative area | thickness [µm] | $R_T$ [K W$^{-1}$] |
|---|---|---|---|---|
| ceramic | 20 | 1/3 | 200 | 0.15 |
| glue 1 | 0.8 | 1/3 | 100 | 1.91 |
| PCB | 3 | 1 | 1600 | 2.72 |
| glue 2 | 0.8 | 1 | 100 | 0.64 |
| Cu-Strip | 300 | 1 | 1000 | 0.02 |

Table 4.2: Estimation of the thermal resistance of the individual slices of the setup.

- the temperature of the resistor can only be estimated from previous measurements
- the fraction of the 1 W power source that is actually dissipated by thermal conductance via the PCB piece is not known.

It is expected that the thermal resistance decreases with increasing number of vias, which it does as shown in figure 4.9. The fact that the measured values are systematically too small for low numbers of vias is probably related to the thermal glue, which most likely filled some vias during gluing, replacing the air and thus decreasing the PCBs thermal conductance. This effect is less severe for larger numbers of vias, since in that case the same amount of glue has to fill more holes. Nevertheless, the $1/\lambda$ dependence of the thermal resistance further confirms that the addition of more vias yields only diminishing returns.

The printed circuit boards used in this thesis have accordingly been designed with a via density of about 15 vias per 2 cm$^2$.

### Temperature difference needed to remove 1 W from a Timepix chip

In order to to design a cooling system of reasonable proportions, one needs to know the temperature difference $\Delta T_c$ needed to fully remove the produced heat from the Timepix chip. Assuming an Octoboard has a similar thermal resistance as the via experiment described above, $\Delta T_c$ can be estimated from that model. One however needs to add the 700 µm Si-layer present in a Timepix chip. Under these assumptions, the thermal resistance between power resistor and copper cooling is about $R_T = R_{\text{via}} + R_{\text{Si}} = 5\,\text{K W}^{-1} + 2.5\,\text{K W}^{-1} = 7.5\,\text{K W}^{-1}$, which, solving equation 3.4 for $\Delta T$, and for a

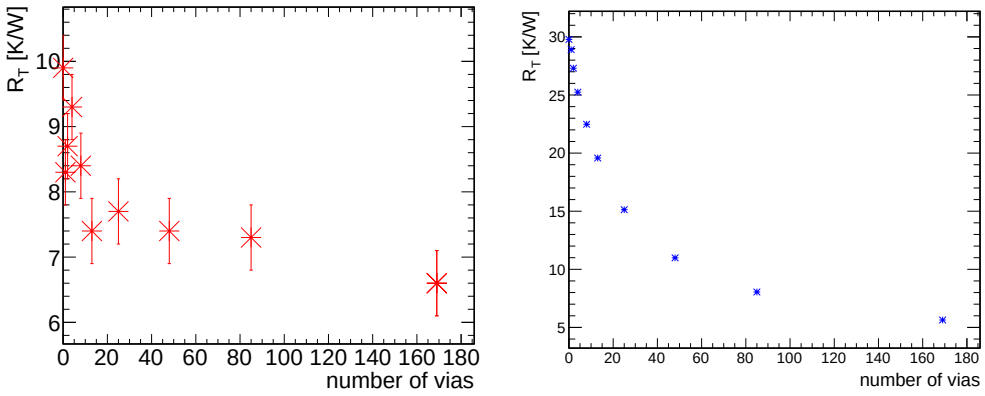


(a) (b)

Figure 4.9: Thermal resistance in dependence of the number of vias a): Measured. b): Computed.

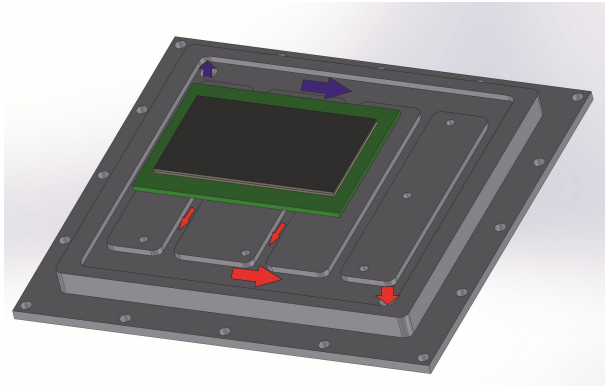

Figure 4.10: Cooling of the LP module. The black objects represent the eight Timepix chips, the green shape is the PCB they are mounted on. The arrows indicate the flow of the cooling water, blue denoting cold and red heated water.

power source of 1 W, yields a temperature difference of 7.5 K:

$$\Delta T_c = \frac{d}{A\lambda}\dot{Q} = R_T \cdot \dot{Q} = 7.5\,\mathrm{K}. \tag{4.4}$$

However, the Timepix has a highly polished and reflective metal surface, which highly promotes emission of heat radiation. According to equation 3.1, the emission of heat radiation is dependent on the emitter surface temperature as $\dot{Q} \propto T^4$. Thus, for a realistic cooling system for a future large scale module, the coolant should be cold enough to cool the Timepix chips to the lowest reasonable temperature, the gas temperature. This was not realized in this thesis, since anything more sophisticated than a water cooling system would have required a substantial effort at the Testbeam site.

### Cooling system

A water cooling system was designed to gather first experience. Cooling conduits were cut into the aluminium cooling unit, see figure 4.10. The cooling conduits are designed in such a way that the summed water flux through all parallel conduits is always the same as the sum over the flux through all

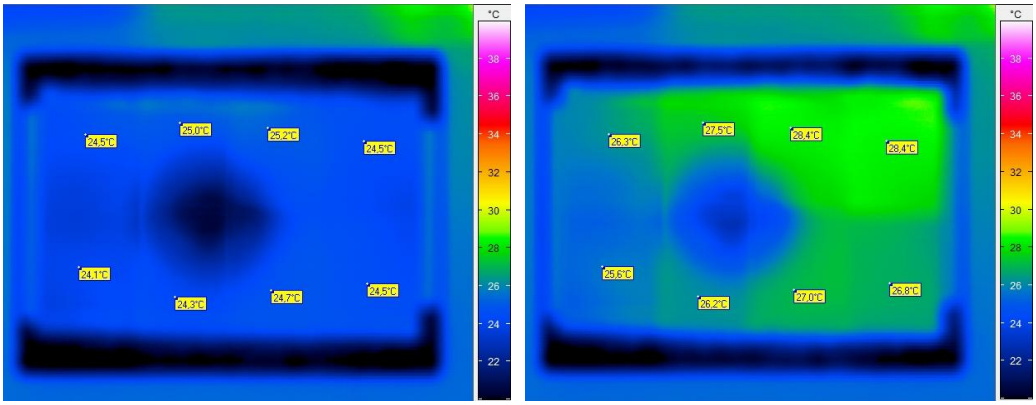


(a) (b)

Figure 4.11: Thermographic images of an Octoboard. The dark dot in the centre stems from reflections. a) Idle Octoboard at room temperature. b). Octoboard under full load.

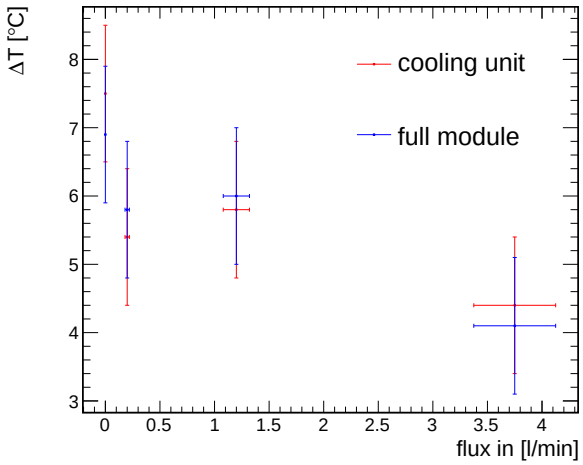


Figure 4.12: Results of the cooling test.

perpendicular conduits. This is necessary to avoid turbulent currents, which would degrade the cooling efficiency as discussed in section 3.2.

### Test of the cooling system

In order to asses to cooling power of the cooling system, tests were performed. An Ocotoboard was installed in the cooling unit, and the temperature of the module was monitored with a thermographic camera, under full load of the Octoboard, using four different coolant flow rates. Mains water was used as coolant. Images of the heated and cooled Octoboard are presented in figure 4.11. The experiment was repeated with the cooling unit installed in the LP module, in order to determine the amount of extra cooling provided by the larger aluminium frame, which acts as a radiator. Figure 4.12 summarizes the results of the cooling test. It can be seen that the difference in cooling power between the cooling unit and the full module is negligible, the cooling provided by the coolant flux is clearly dominant. Uncooled, the Octoboards temperature rises by about 7 °C when under full load. As the coolant flow is increased,

this rise in temperature diminishes to about 4 °C at a flux of 3.75 L min$^{-1}$. While the cooling system halves the excess surface temperature of the Octoboard, it does not keep said temperature constant. The effect of the cooling system on the rest of the module is much more severe, the whole module was cold to the touch while the cooling system was active. The reduced effect on the Octoboard surface is due to its highly reflective nature, making it an excellent emitter for heat radiation. Thus, a large portion of the produced heat, apparently about 50 %, are radiated of instead of dissipated into the module bulk via thermal conduction. This further stresses the aforementioned need for a better coolant than water in a full scale module.

### 4.3.3 Module layout

The LP modules with InGrid and GEM gas amplification structures are very similar in design, which is why in the following a general LP module are described, and if necessary the individual differences of InGrid and GEM modules are pointed out.

The LP modules consist of two major parts. One is the cooling unit carrying both the adapter board and the Octoboard as well as the cooling conduits and connectors. The other is the module bulk, containing the LP frame, the glued-on anode endcap and a rack of HV-connectors. The latter is needed for the InGrid grid voltage and the GEM voltages, respectively.

Top and exploded views of both modules are presented in figure 4.13. The most notable difference is that the GEM module has an additional component, the triple GEM stack, while in the InGrid module the gas amplification structures are included on the Octoboard. Also, due to the larger Octoboard sizes in the InGrid module because of the additional HV-connectors, the Octoboard is rotated by 90° with respect to the GEM modules Octoboard. The cooling conduits (as depicted in figure 4.10) look alike for both modules and are on the rear side of the right hand side aluminium part in figures 4.13b and 4.13d.

The cooling unit is mounted on the module frame (the left hand side aluminium part in figures 4.13b and 4.13d). On its rear side the anode endplate is glued on, and connected to the HV connectors.

### 4.3.4 Module electronics

Two electronic boards are part of the LP module, an Octoboard carrying the chips, and an intermediate board responsible for communication with the readout system and power supply.

An Octoboard is an eight-chip board carrying eight daisy-chained Timepix chips. The board has then a total dimension of $(65.5 \times 45)\text{mm}^2$, allowing for a theoretical maximum of 12 boards or 96 Timepix chips per module. Photographs of the InGrid octoboard are presented in figure 4.14. The Octoboard cannot directly communicate with the readout system, but is connected to a intermediary board, which is located on the side of the LP module not facing the detector volume, by 3 (1 for the GEM Octoboard) pin connectors. The intermediary board is a relatively simple connector, handling data flow from and off the board as well as power supply. The central pin connector delivers the power to the Timepix chips and handles the data, while the two outer connectors supply the HV for four InGrids, each. The latter are not present on the GEM Board, apart from that, it is identically to the InGrid intermediary board, though a bit smaller. An image of the rear side of the Octoboard with all the connectors visible is shown in figure 4.15.

### 4.3.5 Manufacturing

The aluminium parts and the anode plates were manufactured at the university workshop and an external contractor by CNC milling. The cooling unit was manufactured in two parts, a bulk part holding the

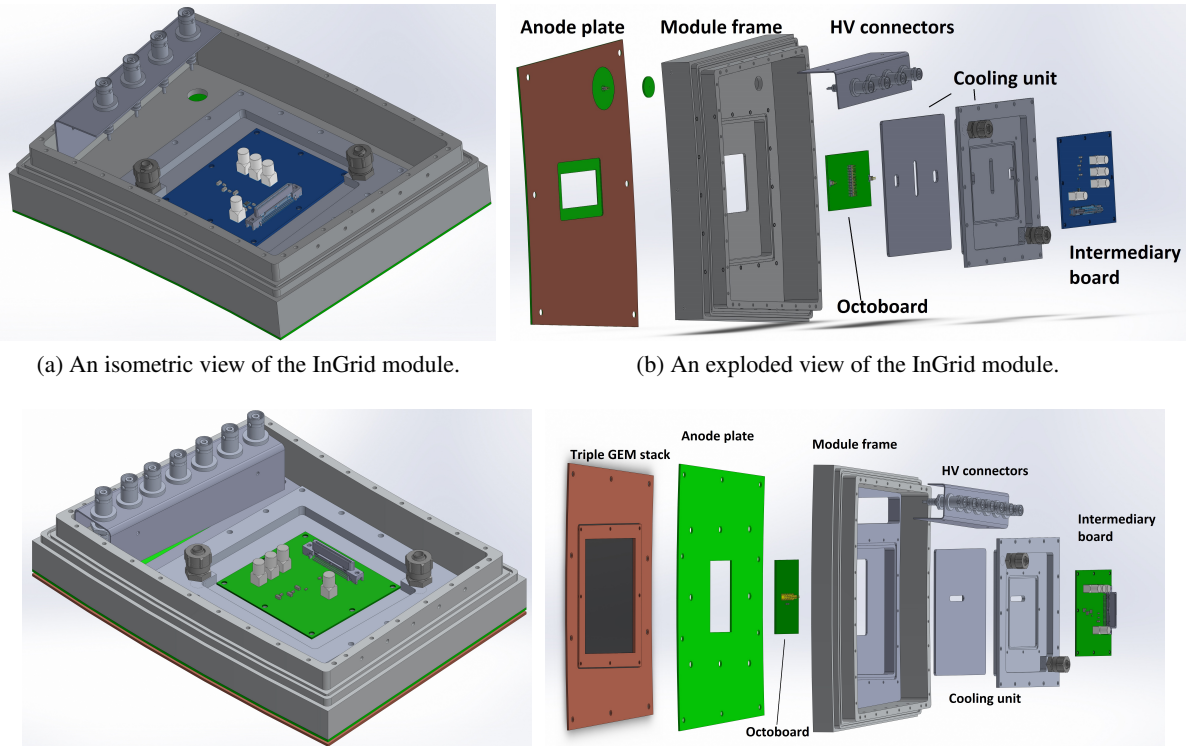


(a) An isometric view of the InGrid module.

(b) An exploded view of the InGrid module.

(c) An isometric view of the GEM module.

(d) An exploded view of the GEM module.

Figure 4.13: Left: Isometric views of the modules. Right: Exploded views of the modules.

cooling conduits, and a cap which was later diffusion-welded to the bulk, sealing the conduits. This welding was done at the Jülich research centre. The welding technique works by pressing the parts together under high temperature, reaching a very high weld joint quality. Unfortunately, the parts became deformed during the process, which could be corrected but rendered the cooling system in-operational in case of the InGrid-module and made it necessary to glue the cooling units onto the module frames, making it impossible to remove the electronics while the modules are installed at the LP, as initially intended.

## 4.4 The Scalable Readout System

The Scalable Readout System (SRS) is a modular readout system developed within the RD51 collaboration. The goal of the project is the design of a readout system that can be used for many different detectors, eliminating the need to develop a new readout system for every new detector. The system is divided into several parts. In our case, a PC was connected to the FPGA based Front-End-Card (FEC). The current iteration of the FEC uses a Xilinx Virtex 5 vlx50t FPGA. The FEC is the same for any application, and is connected to a user designed adapter card, which handles data traffic to and from the detector. Both are mounted in a Eurocrate, and one can simply enlarge this setup until the required number of channels is reached. For large systems with more than 16k channels a Scalable Readout Unit (SRU), which can bundle up to 40 FECs is available [43]. Based on the work presented in [44], an adapter card and FPGA code to communicate with Timepix chips are under development in Bonn. Images of the SRS used at the testbeam are presented in figure 4.16.

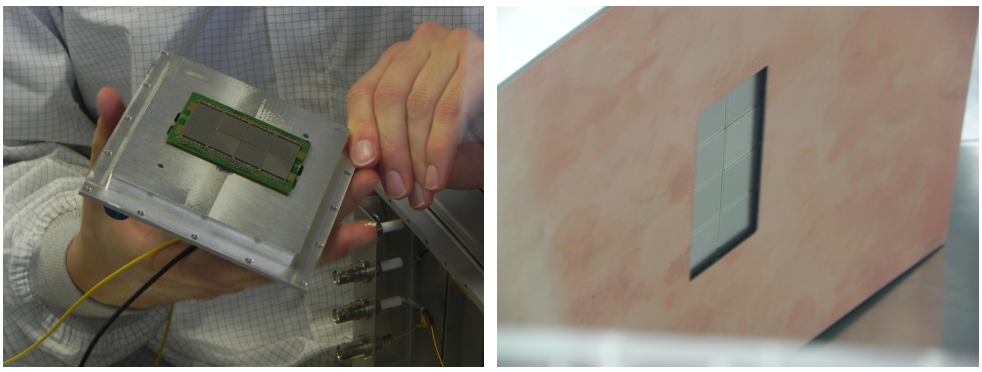

(a) Octoboard installed on the cooling unit. (b) Octoboard in the fully assembled module.

Figure 4.14: Images of the InGrid octoboard

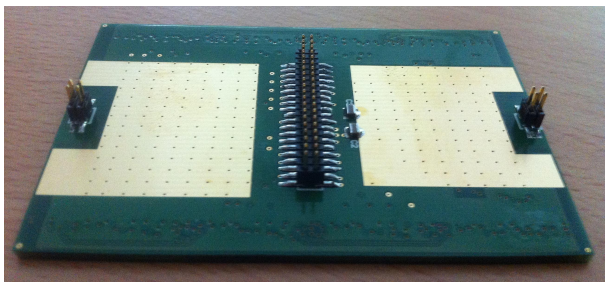

Figure 4.15: Connectors on the rear side of the Octoboard. The outer connectors are for the InGrid HV, while the central connector is used for communication between the Timepix chips and the readout system.

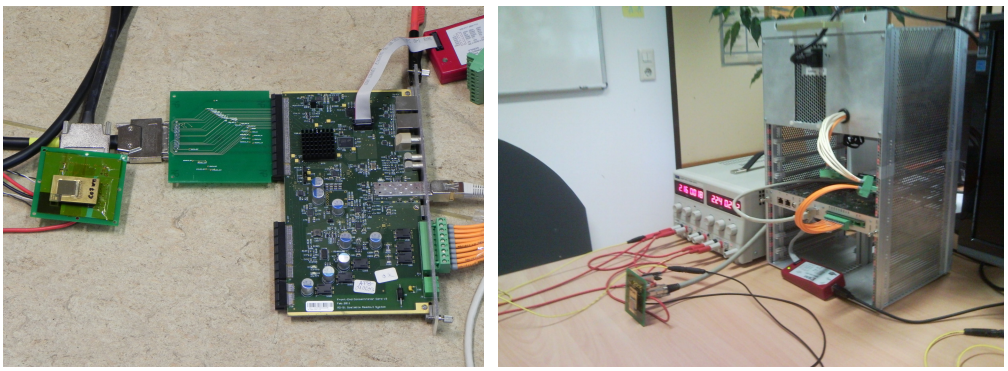

(a) The intermediary board holding a one-chip Timepix carrier board. (b) SRS packed in its Eurocrate.

Figure 4.16: Images of the SRS used at the testbeam. [37]

| $E_{\text{Drift}}$ in V cm$^{-1}$ | $B$ in T | $v_{\text{Drift}}$ in µm ns$^{-1}$ | $D_T$ in µm/$\sqrt{\text{cm}}$ | $D_L$ in µm/$\sqrt{\text{cm}}$ |
|---|---|---|---|---|
| 230 | 0 | 75.84 ± 0.03 | 311 ± 17 | 233 ± 9 |
| 230 | 1 | 76.02 ± 0.03 | 94 ± 6 | 223 ± 10 |
| 130 | 0 | 55.20 ± 0.04 | 314 ± 20 | 314 ± 13 |
| 130 | 1 | 55.26 ± 0.03 | 75 ± 4 | 330 ± 23 |

Table 4.3: Drift and diffusion properties of T2K according to Magboltz [46] from [47].

| Designation | $E_{\text{Drift}}$ in V cm$^{-1}$ | $U_{\text{Grid}}$ in V | B in T | Timepix mode | z in mm | Included |
|---|---|---|---|---|---|---|
| Voltage Scan | 230 | 290-390 | 0 | ToT | 20 | yes |
| Anode Scan | 230 | 350 | 0 | ToT | 20 | no |
| Z scan | 230 | 350 | 0 | ToA | 10-560 | yes |
| Z scan | 130 | 350 | 1 | ToA | 10-560 | yes |
| Z scan | 230 | 350 | 0 | ToA | 10-560 | yes |
| Z scan | 130 | 350 | 1 | ToA | 10-560 | yes |
| p scan | 230 | 350 | 1 | ToA | 20 | no |
| Z scan | 130 | 350 | 1 | ToA | 0-560 | no |

Table 4.4: Summary of InGrid datasets taken during the 2013 testbeam.

## 4.5 Testbeam Campaign

During March and April 2013 the module was installed at the LP module at the LCTPC Large Prototype at DESY, Hamburg. After initial deployment and installation of our equipment, about one million events were recorded over three weeks of nearly continuous data-taking. The InGrid module was installed first, from the 23rd of March until the 2nd of April. The GEM module was installed from the 3rd or April until the 7th of April.

### 4.5.1 T2K gas

During the testbeam, the T2K gas (named after the T2K [45] experiment in Japan), was used as TPC gas. It is a mixture of Ar, $CF_4$ and $iC_4H_{10}$ in the ratio 95:3:2. An overview of its drift and diffusion properties under the influence of different electrical and magnetic fields is given in table 4.3. In the simulations, temperature and data on impurity contamination (c.f. figure 4.17) recorded during data taking was accounted for.

### 4.5.2 Recorded Datasets

The initial analysis performed within the scope of this thesis covers not all datasets. Nevertheless all datasets are listed in tables 4.4 and 4.5. Here it is indicated whether or not a dataset is taken into account.

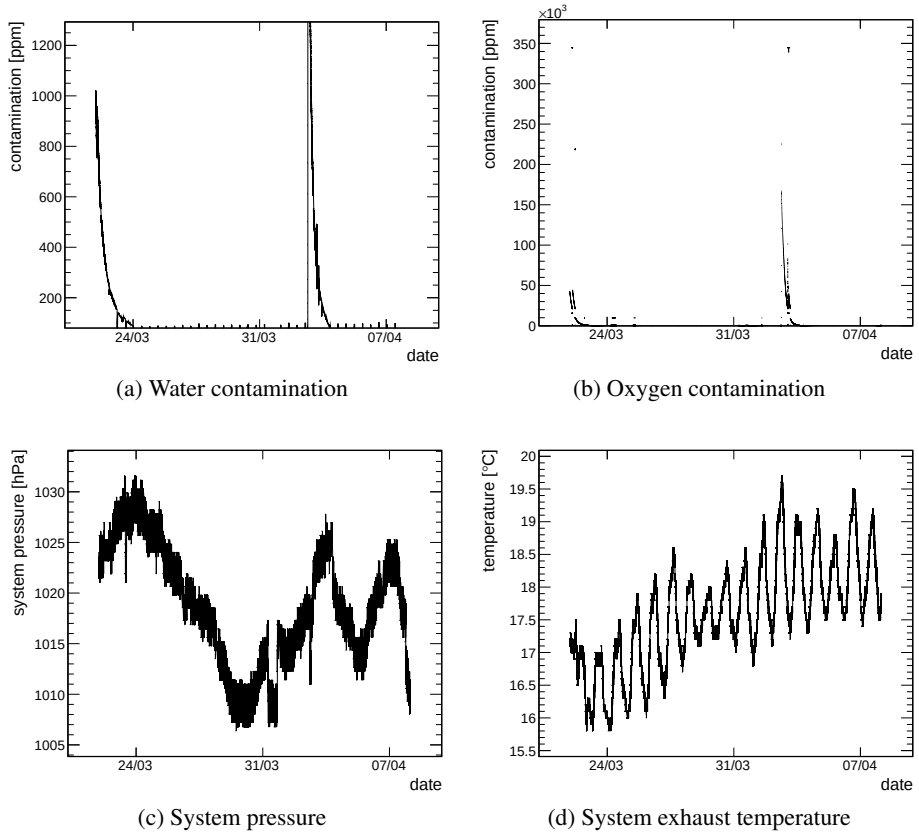


(a) Water contamination

(b) Oxygen contamination

(c) System pressure

(d) System exhaust temperature

Figure 4.17: Contamination and pressure data from the test-beam.

| Designation | $E_{\text{Drift}}$ in V cm$^{-1}$ | $\Delta U$ in V | $B$ in T | Timepix mode | $z$ in mm | Included |
|---|---|---|---|---|---|---|
| Z scan | 230 | 270/275 | 0 | Chess $1 \times 1$ | 0-560 | no |
| $p$ scan | 230 | 270 | 1 | Chess $1 \times 1$ | 20 | no |
| $\varphi$ scan | 230 | 270 | 1 | Chess $1 \times 1$ | 60 | no |
| Z scan | 230 | 270 | 1 | Chess $1 \times 1$ | 0-560 | no |
| Z scan | 130 | 270 | 1 | Chess $1 \times 1$ | 0-560 | no |

Table 4.5: Summary of GEM datasets taken during the 2013 testbeam. The bottom voltage of GEM 3 was 200 V.

# Chapter 5

# Analysis of the data taken during the testbeam-campaign

Within the scope of this thesis, the zscan and voltage runs of the InGrid dataset were analysed. During the voltage scan measurements the chips were set to ToT mode, such that the charge deposited on the chips was measured. This allows to measure the gas gain. During the zscan, the chips were set to ToA mode, allowing for determination of the $z$ position of a hit. This allows full 3D reconstruction of tracks, which is necessary to derive distributions describing the detector performance, especially $xy$ and $z$ single point resolution. Examples for both an InGrid and a GEM event are shown in figure 5.1.

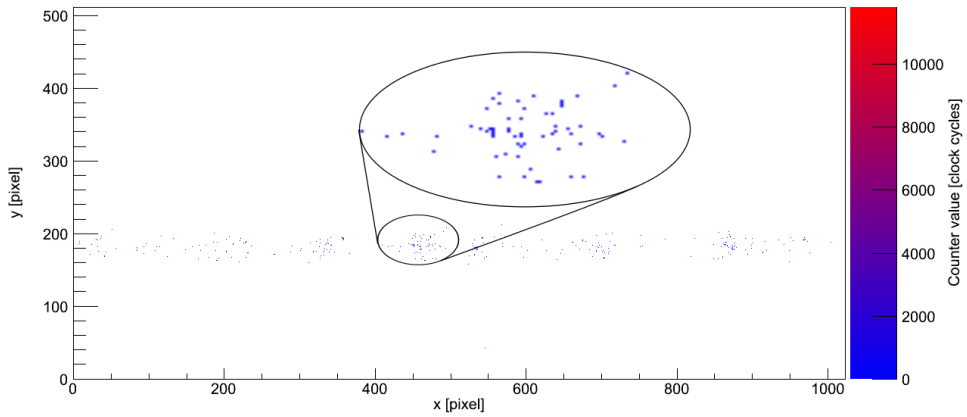


(a) InGrid event.

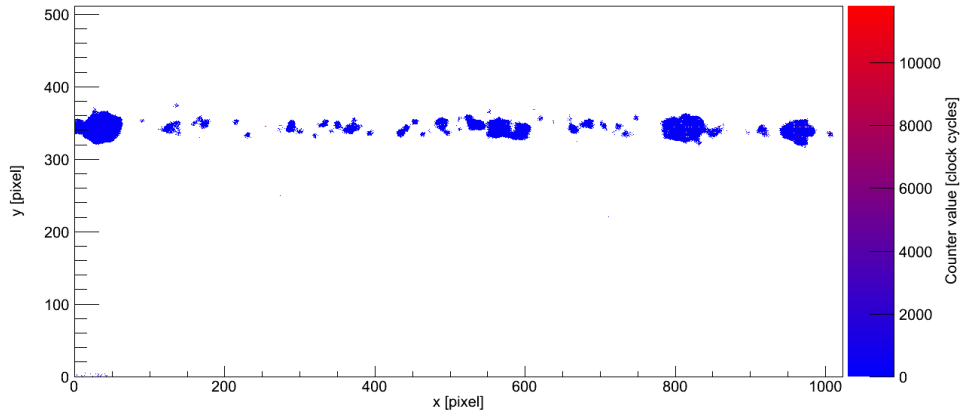


(b) GEM event.

Figure 5.1: Events from the InGrid and the GEM modules.

## 5.1 Analysis software

The analysis discussed in this chapter was performed using the MarlinTPC analysis framework [48],based on Marlin (Modular Analysis and Reconstruction for the LINear collider [49]), which is a common analysis framework used by the research groups working towards a future linear collider. MarlinTPC was developed to provide a unified general approach to data analysis, allowing for exchange of code and comparison of data. To be suitable for the individual needs of different projects, MarlinTPC is highly modular. Different modules, called processors, are available for different tasks, ranging from data read-in to track finding. MarlinTPC feeds one event after the other to the processor chain defined by an XML steering file. Data storage and transfer between processors is conducted in the LCIO (Linear Collider Input/Output) format [50]. Geometry information regarding Pad/Pixel positions is handled by GEAR (GEometry Api for Reconstruction).

The analysis chain in MarlinTPC is usally divided into four steps. First the data is read in and converted from raw data format to LCIO, if the readout system does not directly store the recorded data in LCIO format. Also, if not performed by the readout system, zero-suppression is applied. The second step is data calibration (only for ToT measurements). Then, in a third step, the actual track reconstruction is done. Here, the data is refined into individual hits, which is a very simple process for InGrid data as each pixel corresponds to one hit. Then a Hough-transformation is applied to identify hits forming one track. Eventually, a linear regression is used to calculate the track parameters. In a last step, the detector performance is extracted from the reconstructed data.

In MarlinTPC, most of the reconstruction and analysis software was available and could be used in this analysis. However, especially for data-read-in and hit-finding, several processors had to be changed or even newly developed to deal with the eight-chip board. All used processors are described in appendix A.2.

## 5.2 Octoboard Geometry

The geometry information of the relative position of each pixel towards one another and relative to an arbitrary origin is handled by GEAR. The system requires an XML file which defines the detector geometry. As GEAR is designed for pad readout, the smallest units available are pads, thus, a Timepix chip is represented as a detector module with $256 \times 256$ pads representing the pixels. In order to create an accurate representation of the Octoboard in GEAR, the 3D positions of the four corner pixels of each chip have been measured with a microscope to an accuracy of several micrometers. A graphical representation of the resulting GEAR geometry is presented in figure 5.2.

## 5.3 Occupancy map

The first analysis step was the creation of an occupancy map, which shows how often a pixel was activated in a given dataset. If one uses a large dataset to create this map, one expects a Gaussian distribution with the beam being in the center. This way, defects can be detected, and alignment can be checked. Such an occupancy map was created from 30000 events for the InGrid octoboard, and is shown in figure 5.3. One can clearly see the beam was adjusted above the lower chip row. Besides, some grid defects are visible. The different edge shapes are due to field inhomogeneities. One also notices the lower left chip (chip 1) has a higher occupancy than for example the lower right chip (chip 4). This is due to different thresholds and gas gains of the chips.

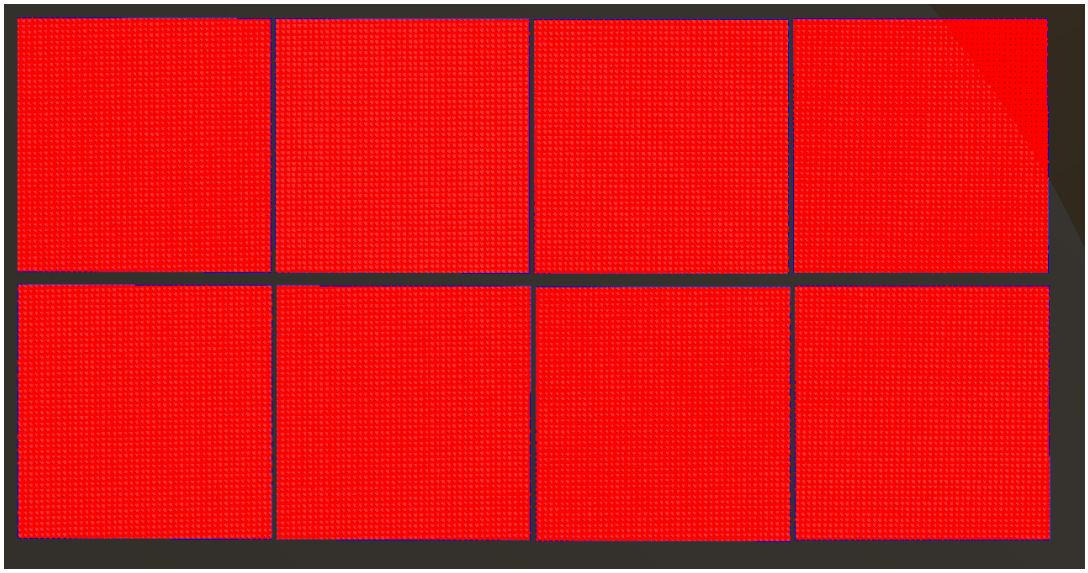

Figure 5.2: Octoboard geometry in GEAR.

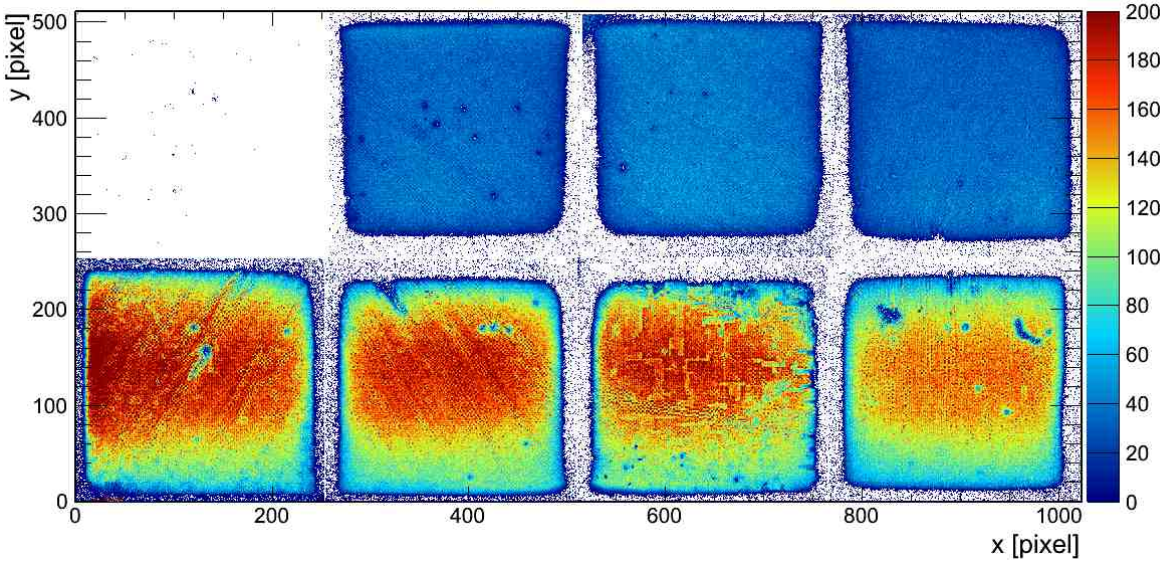


Figure 5.3: Occupancy map of the InGrid Octoboard.

## 5.4 Octoboard field simulations

One also notices, that the occupancy distribution around those chip edges, which are facing the inner side of the Octoboard, are rounder than around the outer edges (c.f. figure 5.3). It is assumed this is due to $E$-field distortions close to the InGrid. This assumption is confirmed by electron deposition simulations performed by [51], shown in figure 5.4a, which show this very same feature.

These simulations took into account the electric field based on the actual measured Octoboard geometry.

If one has a look at the voltage distribution on the Octoboard surface, shown in figure 5.4b, the reason for the round edges in the occupancy-distribution is immediately clear. The voltage, and thus the field, in the center of the crossings between four chips is significantly lower than the field in the gaps between two chips. Thus, the electrons are sucked away from these areas, to the higher field closer to the chip centres. This can be seen quite well if one overlays both the field and occupancy simulations, as done in figure 5.4c.

## 5.5 Data processing

In this section the conversion of ADC counts to physical quantities is discussed.

### 5.5.1 ZScan

The ToA counts $n$ recorded by the readout system can be converted to drift times $t_d$ according to

$$t_d = d + t_{\text{Shutter}} - \frac{n}{f_{\text{Clock}}} \tag{5.1}$$

$$= d + t_{\text{Shutter}} - n \cdot T_c, \tag{5.2}$$

with the trigger delay $d = 108\,\text{ns}$ and the clock period $T_c = 1/f = 25\,\text{ns}$. The shutter time is $t_{\text{Shutter}} = 293.25\,\mu\text{s}$.

The beam/TPC positions, which have a constant offset defined by the LP geometry, also have to be converted to drift lengths. This is done by applying a linear fit to the data and then offsetting the $x$-axis such that the $y$-intercept becomes zero, which is sensible as one knows that for drift length zero the drift time will also be zero. An example for the original and the corrected data is shown in figure 5.5.

#### Drift velocity

Plotting the converted means for all $z$-positions of a zscan dataset versus the drift length yields a linear dependency according to equation 2.11, and the drift velocity can be obtained by means of a linear fit. Results are shown in figure 5.6.

The magnetic field has no effect on drift properties, which is why only the plots without field are presented. As a cross-check, the drift velocities for all recorded field combinations have been calculated, results are presented in table 5.1. As one can see all results for a given electric field, simulated or measured, are comparable.

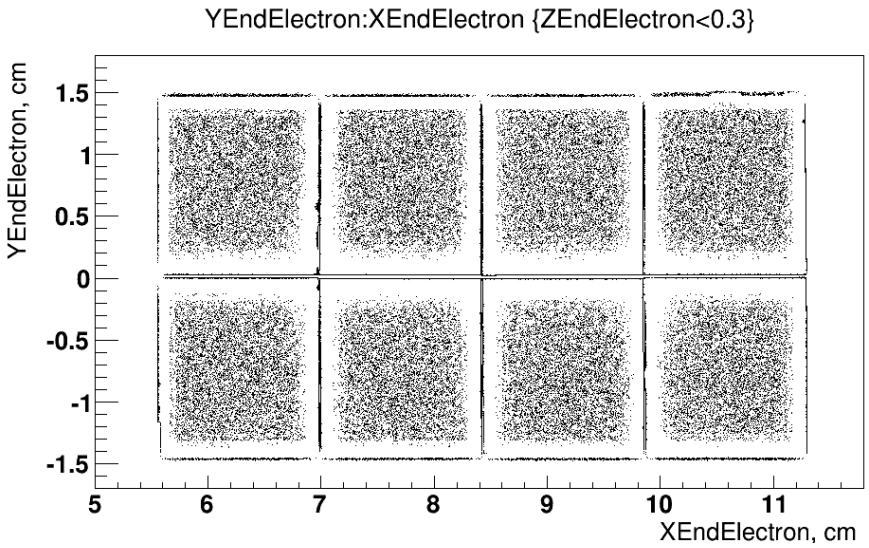


(a) Simulated Octoboard occupancy [51]

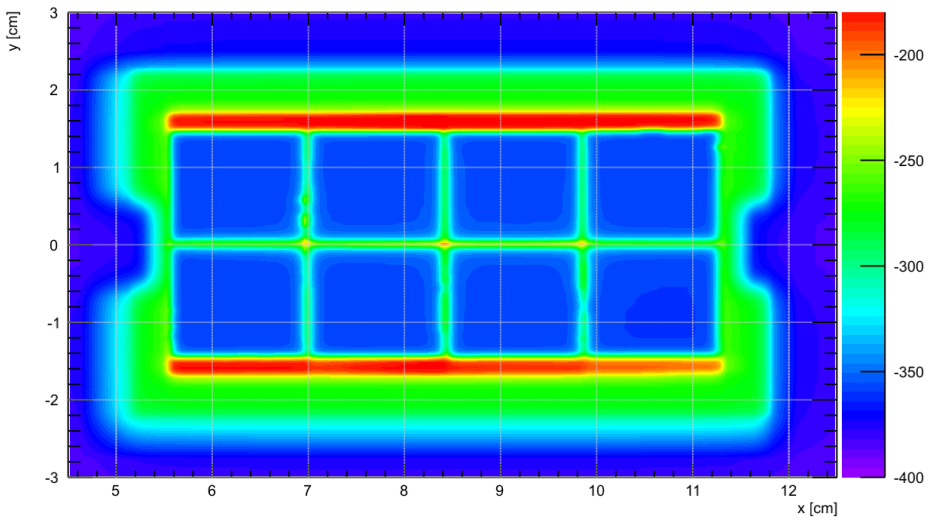


(b) Simulated voltage distribution[51]

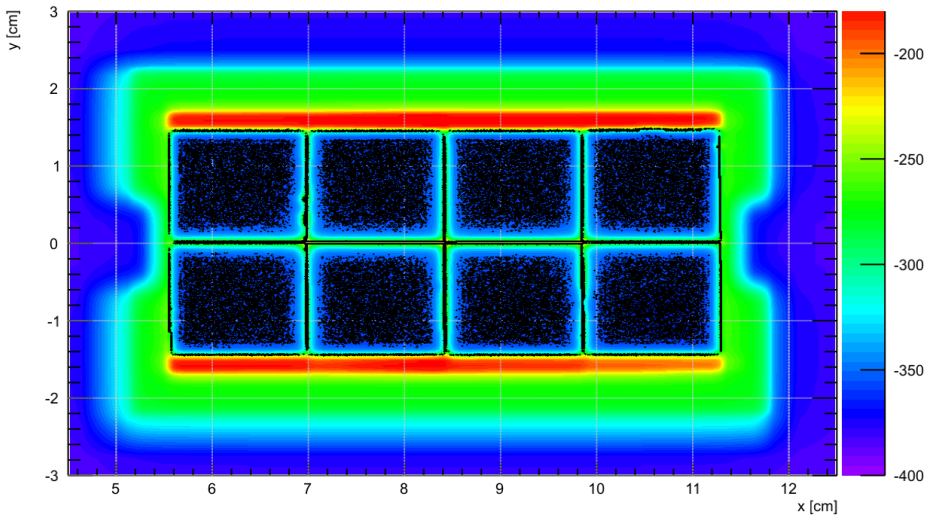


(c) Overlay of both distributions[51]



Figure 5.4: Occupancy and field simulations performed on actual measured geometry data. The red bars in the field simulations mark the chip periphery, while the bump on the $y$-axes is due to the InGrid-HV contacts. [51]

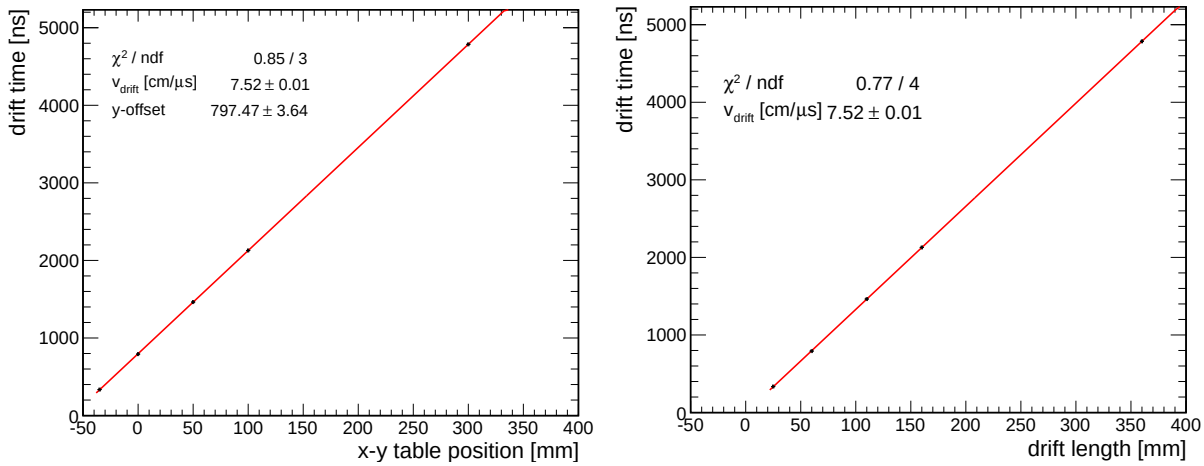


(a) Original data (b) Corrected data

Figure 5.5: Illustration of the TPC position correction. Note that the fit result for the drift velocity does not change.

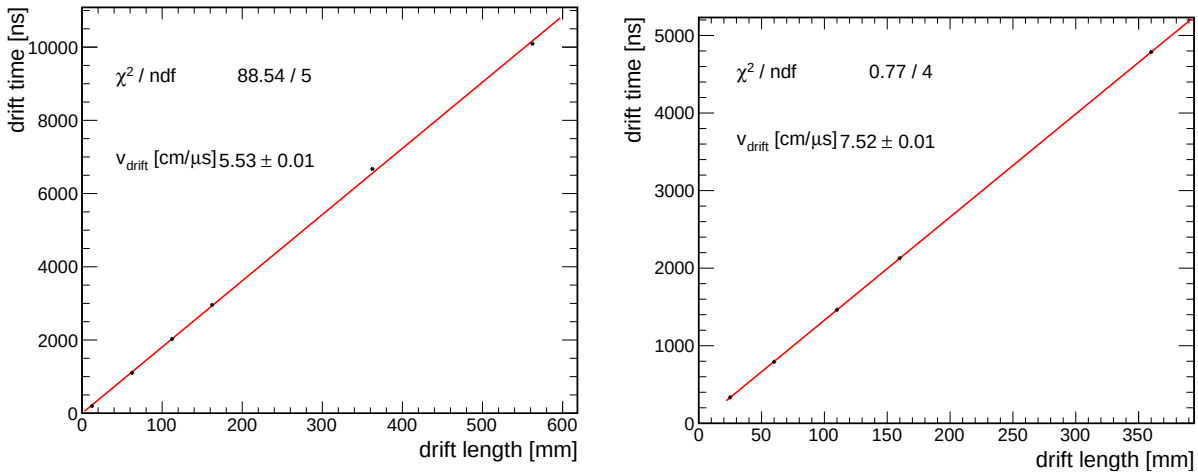


(a) $E = 130 \frac{\mathrm{V}}{\mathrm{cm}}$ (b) $E = 230 \frac{\mathrm{V}}{\mathrm{cm}}$

Figure 5.6: Drift velocities for different drift fields, without magnetic field.

| $B$ in T | $E_{\mathrm{Drift}}$ in V cm$^{-1}$ | $v_{\mathrm{measured}}$ in cm µs$^{-1}$ | $v_{\mathrm{simulated}}$ in cm µs$^{-1}$ |
|---|---|---|---|
| 0 | 130 | 5.53 ± 0.01 | 5.520 ± 0.004 |
| 0 | 230 | 7.52 ± 0.01 | 7.584 ± 0.003 |
| 1 | 130 | 5.46 ± 0.01 | 5.526 ± 0.003 |
| 1 | 230 | 7.33 ± 0.01 | 7.602 ± 0.003 |

Table 5.1: Drift velocities for different electric and magnetic fields.

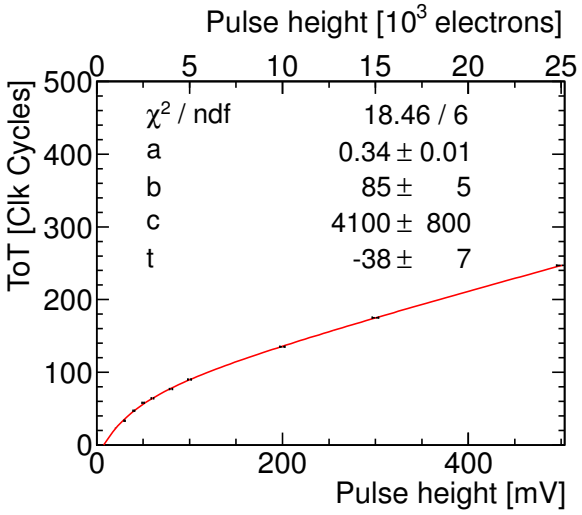


Figure 5.7: Calibration curve for chip 1.

### 5.5.2 Voltage scan

#### Calibration

The information read out from the pixels is measured in clock cycles (ToT counts or TIME counts, depending on measurement mode). To make a further analysis viable, first a calibration as described in [15] is necessary. By plotting the ToT counts versus injected charge, respectively pulseheight, and fitting the calibration function to the data, one obtains its parameters, allowing for conversion of ToT counts to pulse height/input charge. It is assumed that a voltage step of 20 mV corresponds to 1000 electrons [15]. An example for a calibration plot is shown in figure 5.7.

#### Gas gain

By calibrating, the charge in electrons can be computed from recorded TOT counts. As on an InGrid chip it is assumed that every charge deposition stems from a single electron, such that the charge per hit in electrons is equal to the gas gain. This does not take into account charge sharing between pixels. Charge depositions on a pixel may also affect surrounding pixels, and if the portion of charge transferred to a neighbouring pixel exceeds that pixels threshold, it may appear as a disjunct hit. The concept of charge sharing is discussed in [52] The distribution of the gas gain is described by a Polya distribution, with the mean gain being one of the functions parameters (c.f. equation 2.18). Examples for three of the thirteen measured voltages are shown in figure 5.8.

The dip on the leading edge and the spike at the trailing edge of the distribution are present for data from all chips in the lower row and for most voltages. For low voltages they are not visible. For high voltages the dip and the spike are present at the same ToT count values for all chips. The reason for this dip is to this time still unknown, further investigation is needed.

By fitting Polya distributions to the histograms, one can calculate the gas gain, which is a parameter of the Polya distribution. Using data for different InGrid voltages, the dependence of the gas gain of the grid voltage can be obtained. The results for this are shown in figure 5.9. The gas gain rises approximately exponential with the applied voltage.

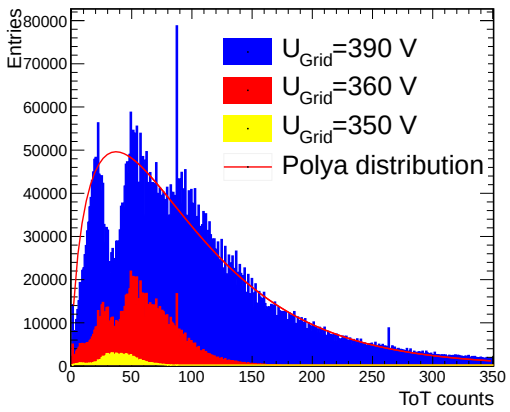


(a) Chip 1

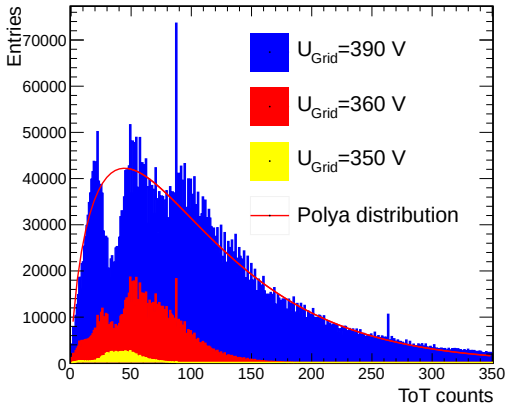


(b) Chip 2

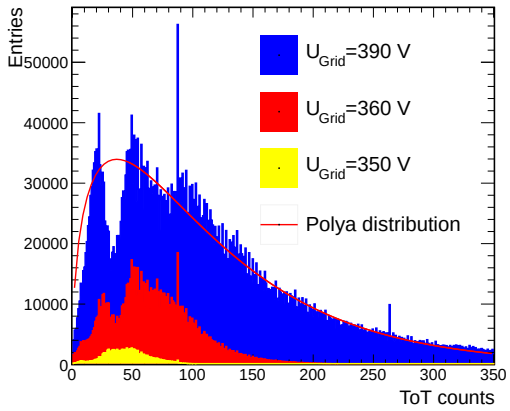


(c) Chip 3

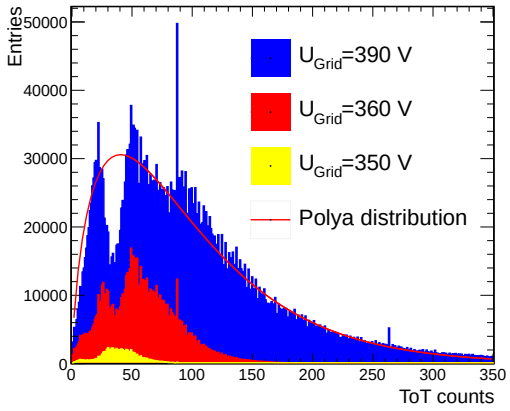


(d) Chip 4

Figure 5.8: Polya distribution of the ToT for the four chips aligned with the beam at different grid voltages. The fit of the Polya distribution shown here was applied to the histograms with $U_{\text{grid}} = 390\,\text{V}$. The fit was performed from around 60 counts to 350 counts.

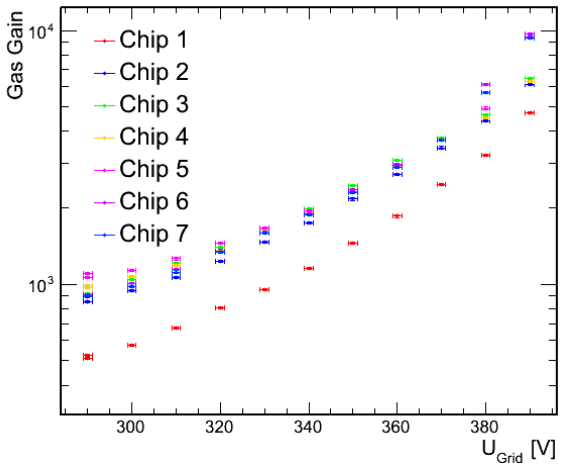


Figure 5.9: Gas gain for all active chips at different grid voltages.

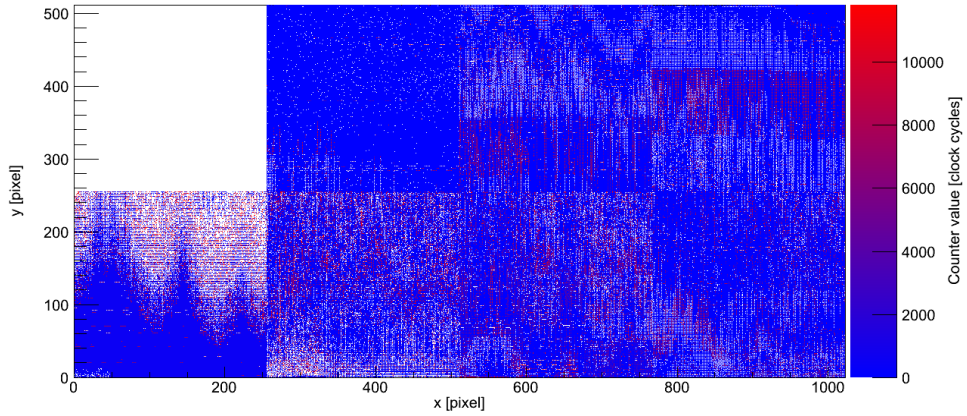


Figure 5.10: Noisy InGrid event.

## 5.6 Data quality

The quality of the data taken during the testbeam campaign was degraded by the issues discussed in the following:

- Chip eight on the InGrid Octoboard was noisy, which is why its threshold was set to a very high value, thus avoiding data-corruption. To still have a maximal active area, the detector was brought into a position were the lower, functional row of the Octoboard collects the charge carriers emerging from the active volume.
- For safety reasons, the SRS crate with the power supply had to be placed several meters away from the magnet during runs in which the magnetic field was turned on. This made longer cables necessary, which, in turn, caused crosstalk in some frames. These were removed from the data-set by a filesize check as described in section 5.6.1. Exemplarily, an effected event from the InGrid dataset is shown in figure 5.10.
- The GEM module kept sparking at GEM voltages above 270 V. This was below the voltage we had hoped to achieve, it is however sufficient for gas amplification, such that data-taking was possible.
- During experimental set-up, the readout system for the PT 100 temperature probes mounted on the modules was damaged, thus a quantitative test of the cooling system was not possible.

### 5.6.1 Data Cleaning

As a first step, noise and other non-physical components of the data are removed.

#### Magnetic field noise

The datasets with applied magnetic field are corrupted due to the longer cables needed. An example for a noisy event is shown in figure 5.10. This noise was removed from the data by a filesize check. There are eight datafiles per event, one per chip. For the filesize check only chip 1 was considered, as the noisy events always affect the whole board. Only those events were selected for analysis, whose raw data filesize was below a certain threshold. The clean datafiles are mostly below 140 kb, while the noisy

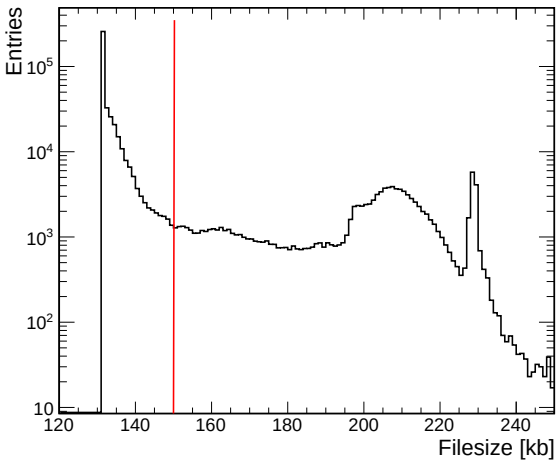


Figure 5.11: Filesize spectrum. The data right hand side of the red line was cut away. The sharp peak at the left hand side of the distribution represents empty frames with only zeros in them.

files are usually above 200 kb (per chip). The threshold was set to 150 kb to avoid removal of good files. This is visualized in figure 5.11.

### Readout system malfunction

Cuts are applied to remove hits which are outside the physical TPC. These are obviously artefacts, since they interfere with the track reconstruction. Even if a track has several hundred hits, a single hit which is a few hundred millimetres away from the track, but incorrectly associated to a track, will severely distort the reconstructed track. This is because the track reconstruction is done by a linear regression as described in section 5.7.1, and the position enters inversely squared into the slope.

**Bit shifts** The non-physical hits from the readout system malfunction, which make up about 3.9 % of the data, stem from errors in the readout-system. The pixel status is stored in its 14-bit counter, if all 14 bits are set to high this corresponds to a zero, while any mixture of highs and lows corresponds to a given number as defined by the lookup-table. An excerpt of the lookup-table is presented in table A.1. In case one pixel is hit, and its neighbouring pixels are not, this would look like Pixel 2 in table 5.2. The counters are readout in rows, meaning the first bits of all counters are read-out at the same time, then in the next cycle the second bits of all counters of pixels in one row are read out and so on. The bits of one row are then chained together one by one and read-out. During this, a bit shift may occur, meaning a bit is mistakenly sorted onto the position of a neighbouring pixels bit. This obviously changes the bit pattern of both pixels. As the physically sensible range for our experiment was about 0-700 counts as explained later, while the readout system can count up to 11800, this easily can produce hits outside the TPC in ToA mode, and non-physical charge value in ToT mode.

**Idle pixel bit-shift** In the aforementioned heavily dominating case that a pixel is hit but its neighbours are not, this would change the high-states-only bit pattern of the pixel that wasn't hit to another pattern, making it appear to be hit. There is a limited amount of numbers possible due to this effect, assuming only one bit is shifted, which are: 0;2;481;3113;4084;6716;8978;11180;11587 and 11590 (some occur more than once). These lead to high one-bin wide spikes in the ToA/ToT spectra shown in figure 5.12.

| | Pixel 1 | Pixel 2 | Pixel 3 |
|---|---|---|---|
| Bit 1 | 1 | 1 | 1 |
| Bit 2 | 1 | 0 | 1 |
| Bit 3 | 1 | 1 | 1 |
| Bit 4 | 1 | 1 | 1 |
| Bit 5 | 1 | 1 | 1 |
| Bit 6 | 1 | 0 | 1 |
| Bit 7 | 1 | 1 | 1 |
| Bit 8 | 1 | 0 | 1 |
| Bit 9 | 1 | 1 | 1 |
| Bit 10 | 1 | 1 | 1 |
| Bit 11 | 1 | 0 | 1 |
| Bit 12 | 1 | 1 | 1 |
| Bit 13 | 1 | 1 | 1 |
| Bit 14 | 1 | 0 | 1 |

Table 5.2: Example for the data-structure in three neighbouring pixels.

An individual spike is shown in figure 5.12e. For the ToT spectrum some of the more visible spikes were marked. The spikes cause about 25 % of the non-physical data in the spectra.

**Active pixel bit-shift** Another 25 % are caused by the lost bits of the actually hit pixels, in which the bit shift originally occurred. In this case, the original bit pattern, corresponding to an ADC value which corresponds to a drift time which would place the hit inside the TPC (in the case of ToA) or a reasonable charge value (in the case of ToT), is modified by one bit leading to a new bit pattern which most likely does not correspond to a physically sensible value. This leads to broader distributions, as the new count value depends on the actually counted value when the pixel was activated. Such a distribution is shown in figure 5.12f.

The origin of the remaining 50 % of the ToA/ToT counts outside the physically sensible range is at this time unknown.

Zooming in on the spectrum three distinct structures become apparent. First the real ToA and ToT spectra on the left hand side of the plots. In the case of ToT data, this is a Polya distibution as shown in figure 5.8. For ToA data, a peak is expected corresponding to $z$-position of the beam, as shown in figure 5.12d. Then there are two different kinds of distortions, single bin spikes which have several thousand entries, and wider distributions, which have a width of several bins, as shown in figure 5.12f.

**Bit shift correction** For time of arrival measurements, the false hits removal is done by the reconstructed $z$-coordinate. The LP has a length of $l = 567.6\,\mathrm{mm}$ so all hits that are outside the range of $0 \ldots l$ obviously are not physical and have to be removed in order to perform a sensible analysis. This is done during read-in of the data from raw data ASCII files to LCIO. The physically acceptable $z$-interval is re-converted to ToA counts to perform this correction on raw data. The upper limit is simply the maximal shutter length in clock counts c.f. equation 5.2, which corresponds to the anode. The lower limit is calculated by first calculating the maximal drift time $t_{\mathrm{max}} = \frac{z_{\mathrm{max}}}{v_{\mathrm{drift}}}$ which then is converted to ToA clock counts using 1 count = 25 ns. This value is then subtracted from the upper limit, yielding a range of $290 \ldots 560$ clock counts for physical data in the case of a drift field of $E_{\mathrm{Drift}} = 230\,\mathrm{V\,cm^{-1}}$.

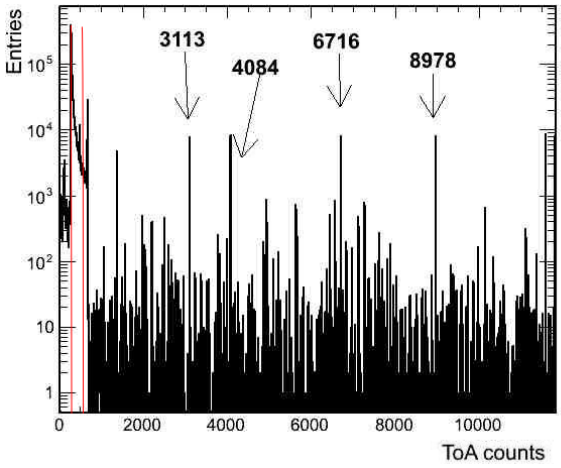


(a) ToA

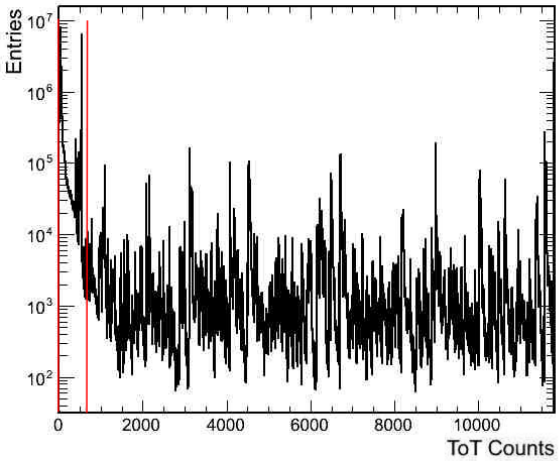


(b) ToT

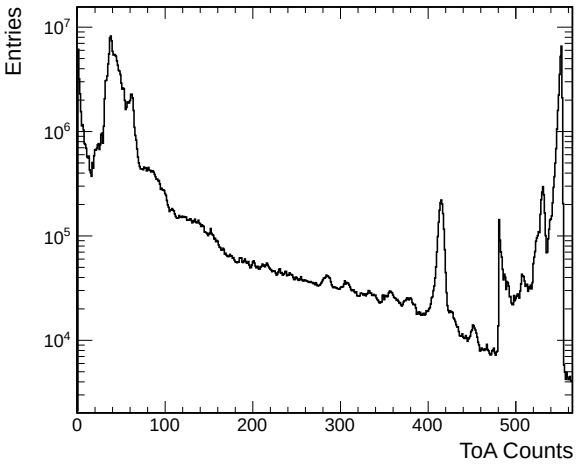


(c) Zoom-in on the physical area the ToA spectrum. The peak at the left side represents the anode, the peak at about 410 counts corresponds to the $z$-position of the beam. The peak on the right side stems from the cathode.

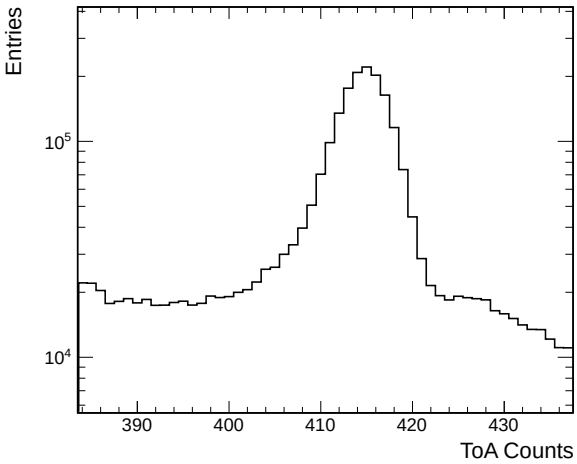


(d) Zoom-in on the beam position peak in the ToA spectrum

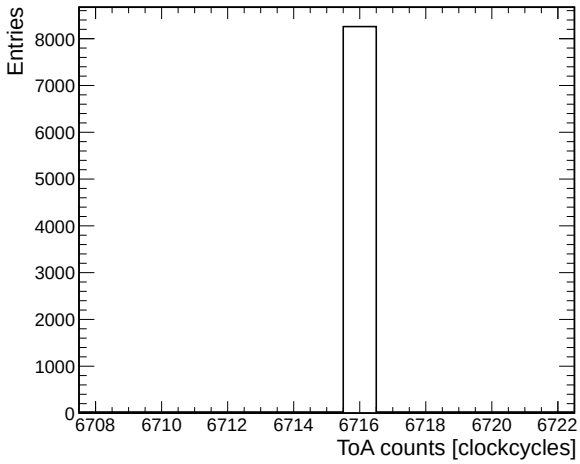


(e) Example from a spike caused by bitshift.

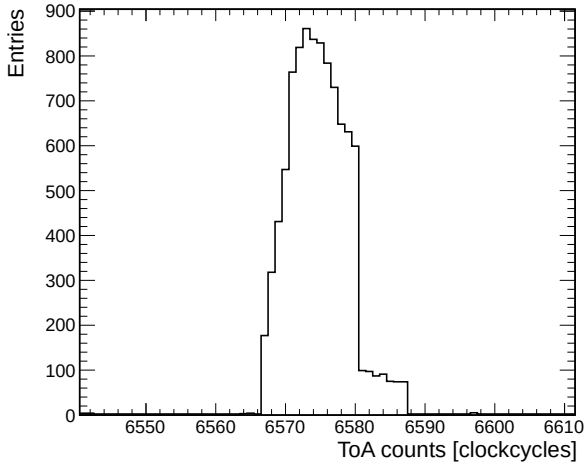


(f) Example for a distribution caused by bitshift.

Figure 5.12: ToA and ToT spectra in logarithmic scale.

An analogous correction is applied on ToT data, yielding an acceptable range of $0 \ldots 700$ counts. In both cases, all counter values outside these ranges are set to zero. These are removed from the data during zero-suppression, thus, this does not affect the analysis.

### 5.6.2 Data Selection

Only the part of the sample remaining after cuts is used for the analysis. The cuts are meant to select a data sample with straight, correctly reconstructed single tracks parallel to the board axis without any anomalies. Applied cuts are shown in figure 5.13. Effects of the cuts are made visible in the consequent analysis whenever sensible

**Number of tracks cut** As the track finder algorithm works only reliable with single tracks, for an initial analysis a data sample only containing single tracks was selected. This also excludes delta electrons from the analysed dataset to some extent.

**Number of hits on track cut** Tracks with a number of associated hits greatly deviating from the MPV usually are either very short or very long, indicating either their $\phi$ or $\lambda$ notably deviates from zero. This usually means only a part of the track was recorded by the active area of the detector, or a second track in the event was not reconstructed. Tracks with a very high number of hits usually originate from two physical tracks which have not been separated properly. To avoid this, cuts have been applied to the outer boundaries of the corresponding Landau distribution.

**Angular and $y$-Position cut** All tracks that cross a line which is three times the average diffusion away from the chip border are removed from the dataset. This runs into a limit at a drift distance of about $z = 56\,\text{cm}$ without magnetic field, as here a track running exactly through the center of the chip would spread across the whole chip within this $3\sigma$ limit. In the case of an active magnetic field diffusion is suppressed and this is not an issue. The reason for this cut is to remove tracks from the dataset which only traverse over a part of the Octoboard. This cut method effectively cuts on both, the mean $y$-position of a track, and on its $\phi$ and $\lambda$.

**Effects of the individual cuts** The individual effects of the aforementioned cuts were studied by applying the cuts to the data one after another. First the number of tracks cut is applied, having the most significant effect. Then $y$-position and number of hits on track cuts are applied. Overall about 50 % of the dataset is discarded. The effects of the individual cuts are visualized using the track distributions in figure 5.14. The percentage of events remaining after the subsequent cuts were:

- Number of tracks cut: 70 %
- Angular and $y$-position cut: 56 %
- Hits on track cut: 51 %

## 5.7 Reconstruction

After calibration and determination of parameters needed for track reconstruction, it is possible to reconstruct full 3-dimensional tracks and to obtain several distributions describing the detector performance, especially the single point resolution. These are discussed in the following.

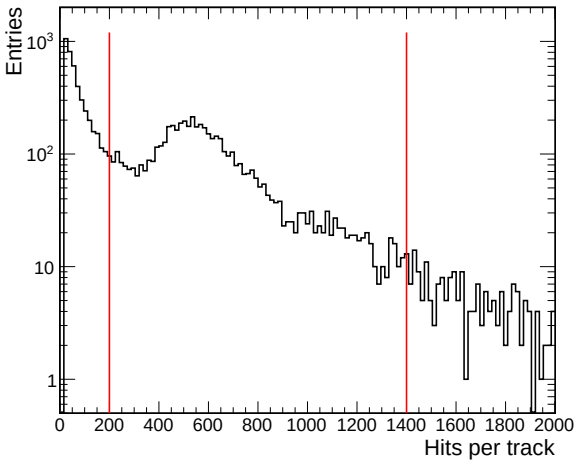


(a) Hits per track

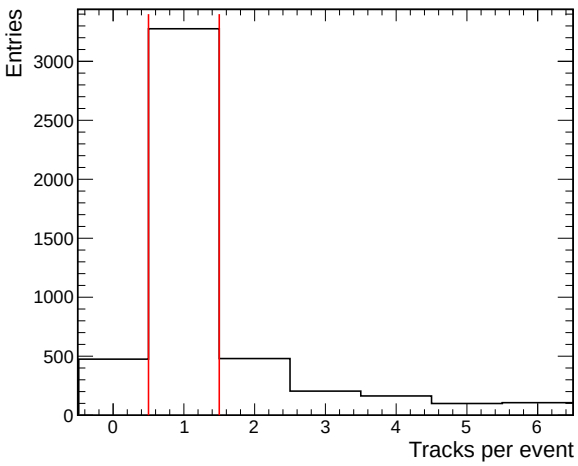


(b) Tracks

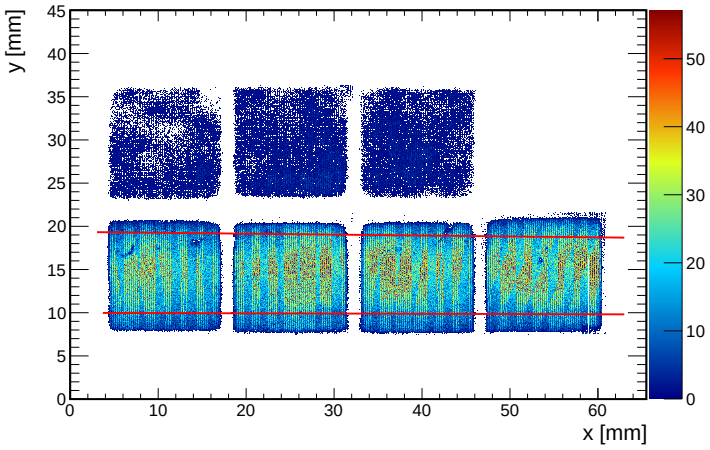


(c) Angle and $y$-position

Figure 5.13: Cuts applied to the raw data. The area inside the two red lines represents the accepted data. In the case of the $y$-position cut, tracks must not cross either line in order to be accepted.

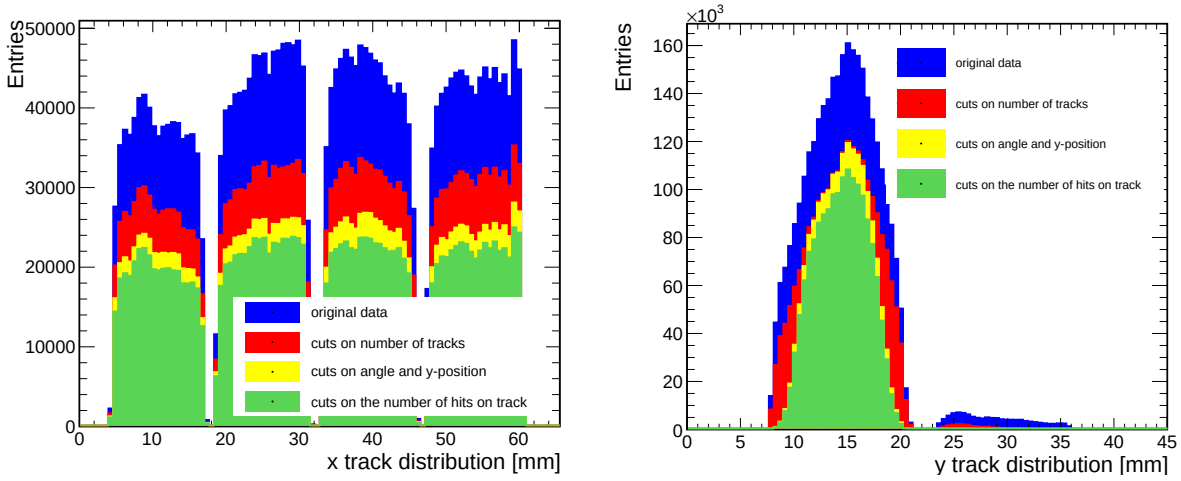


(a) Cut effects on the x track distribution.

(b) Cut effects on the y track distribution.

Figure 5.14: Effect of the individual cuts applied to the data. The coloured areas represent the data remaining after the indicated cut.

### 5.7.1 Track Reconstruction

#### Hough Transformation

To reconstruct tracks from the data, first hits are associated to tracks by means of a Hough transformation [53],[54]. Here, a track containing points $(x_i, y_i)$ which is represented by

$$y_i = m \cdot x_i + b \tag{5.3}$$

gets transformed such that the point coordinates become slope and intercept [55]:

$$b = -m \cdot x_i + y_i. \tag{5.4}$$

This method transforms the orignal image to the Hough space, where every point appears as a line. The point where all these lines intercept gives the line that best matches al points in position-space. Thus tracks are found and the corresponding hits associated to them. These sets of hits are then called track candidates.

#### Linear Regression and track parameter calculation

A linear regression is applied to the track candidates to calculate the track parameters. Slope $m$ and intercept $b$ are calculated according to

$$m_{xy} = \frac{\bar{xy} - \bar{x}\bar{y}}{\bar{x^2} - \bar{x}^2} \tag{5.5}$$

$$b_{xy} = \bar{y} - m\bar{x}. \tag{5.6}$$

This linear regression is performed in the $xy$ and $xz$ (or $yz$) planes independently. The track parameters can then be calculated from the slopes and intercepts:

$$\phi = \arctan m_{xy} \tag{5.7}$$

$$\lambda = \arctan\left(\frac{m_{xz}}{|m_{xz}| \arccos\left(\frac{\sqrt{m_{xy}^2+1}}{\sqrt{m_{xy}^2+,_{xz}^2+1}}\right)}\right) \tag{5.8}$$

$$d_0 = m_{xy} \cdot \cos\phi \tag{5.9}$$

$$z_0 = \frac{m_{xy} \cdot b_{xy} \cdot m_{xz}}{m_{xy}^2 + 1} + b_{xz} \tag{5.10}$$

These four parameters now fully define the track. An example for a reconstructed track is shown in figure 5.15.

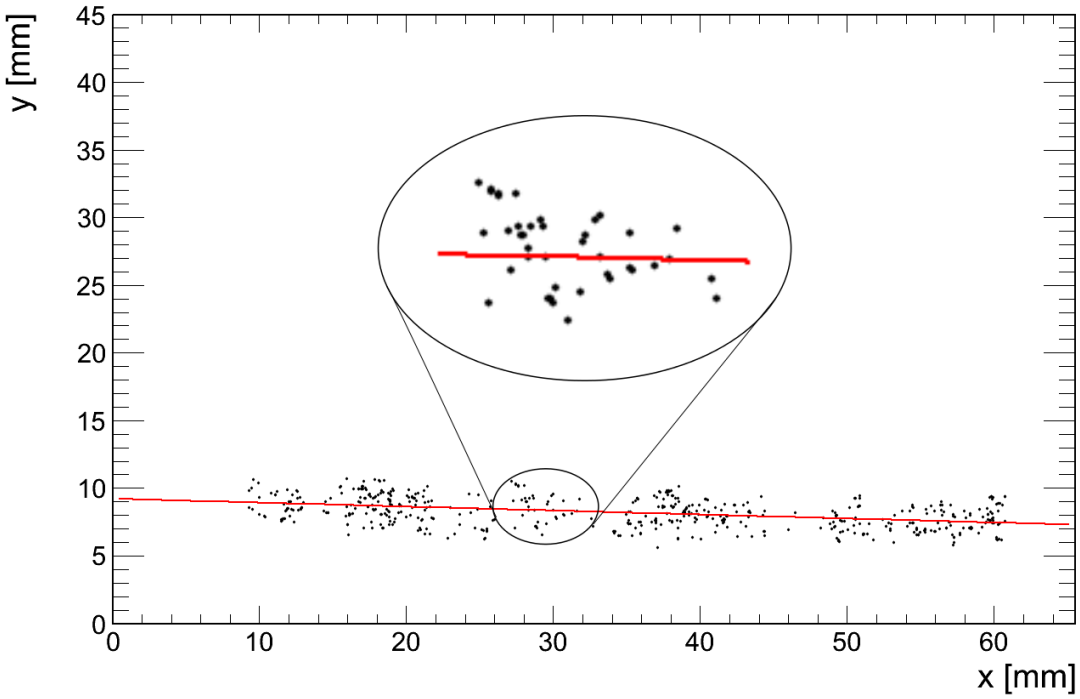


Figure 5.15: Reconstructed hits and corresponding track at an electric field of 230 V cm$^{-1}$.

### 5.7.2 Track Distribution

Since during data taking the Octoboard and electron beam were aligned such that the beam crossed only the four lower chips, a concentration of hits on the lower chip row is expected. In figure 5.16 $x$,$y$ and $z$ track distributions are shown for cut and uncut data. Both are from a run with $E_{\text{drift}} = 230\,\text{V cm}^{-1}$, $B = 0\,\text{T}$ and $z \approx 160\,\text{mm}$. In the $x$ distribution the gap between the chips is clearly visible, the same is true for the uncut $y$ distribution. For cut data the x distribution gets flatter, while the $y$ distributions tails are now fully recorded. For uncut data the tails were truncated, as some tracks were not fully on the active area. This shows the $3\sigma$ $y$-position cut is sensible. The $z$-distribution actually looks alike with and

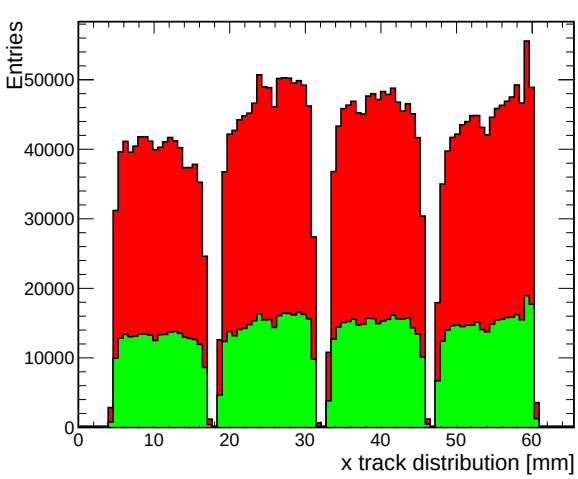


(a) $x$ track distribution

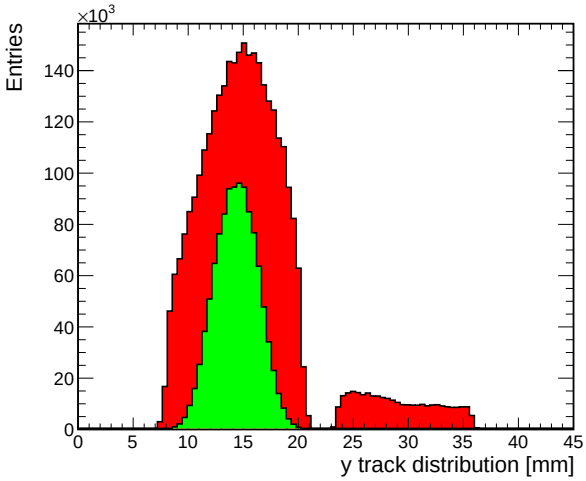


(b) $y$ track distribution

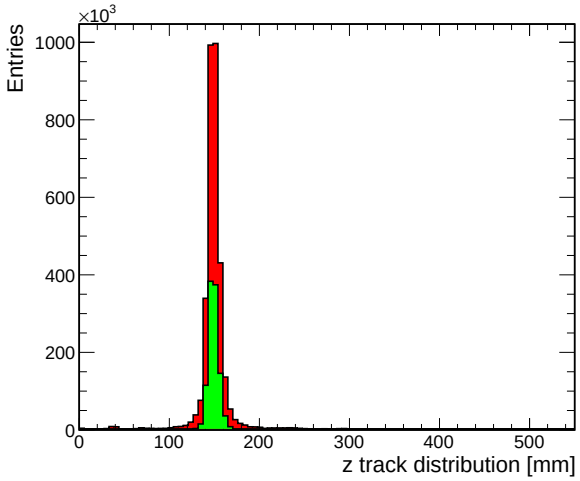


(c) $z$ track distribution

Figure 5.16: $x$,$y$ and $z$ track distributions from a run with $E_{\text{Drift}} = 230\,\text{V}\,\text{cm}^{-1}$, $B = 0\,\text{T}$ and $z \approx 160\,\text{mm}$. The histograms are filled red, while green represents the dataset remaining after cut application.

without cuts, but the number of events is decreased due to the cuts on other quantities. It is a localized peak different from a broad distribution as the data source is a beam other than cosmic radiation or collider events, and the $z$-position of the beam was fixed for this dataset.

### 5.7.3 Track Parameters

As discussed in section 2.4, tracks in a TPC are described by four track parameters, $z_0$, $d_0$, $\lambda$ and $\varphi$. Measurements and expectations will be discussed in this section.

As the x-axis of the Octoboard is assumed to be close to parallel to the beam, $\varphi$ and $\lambda$ are expected to be close to zero. In figures 5.17a and 5.17b one can see this is the case for the cut data. The uncut data shows a considerably broader distribution, which is the reason for the tight $y$-position (and thus angular) cuts which were applied to the data.

As mentioned earlier, the particle source is an electron beam with a certain width at a defined position

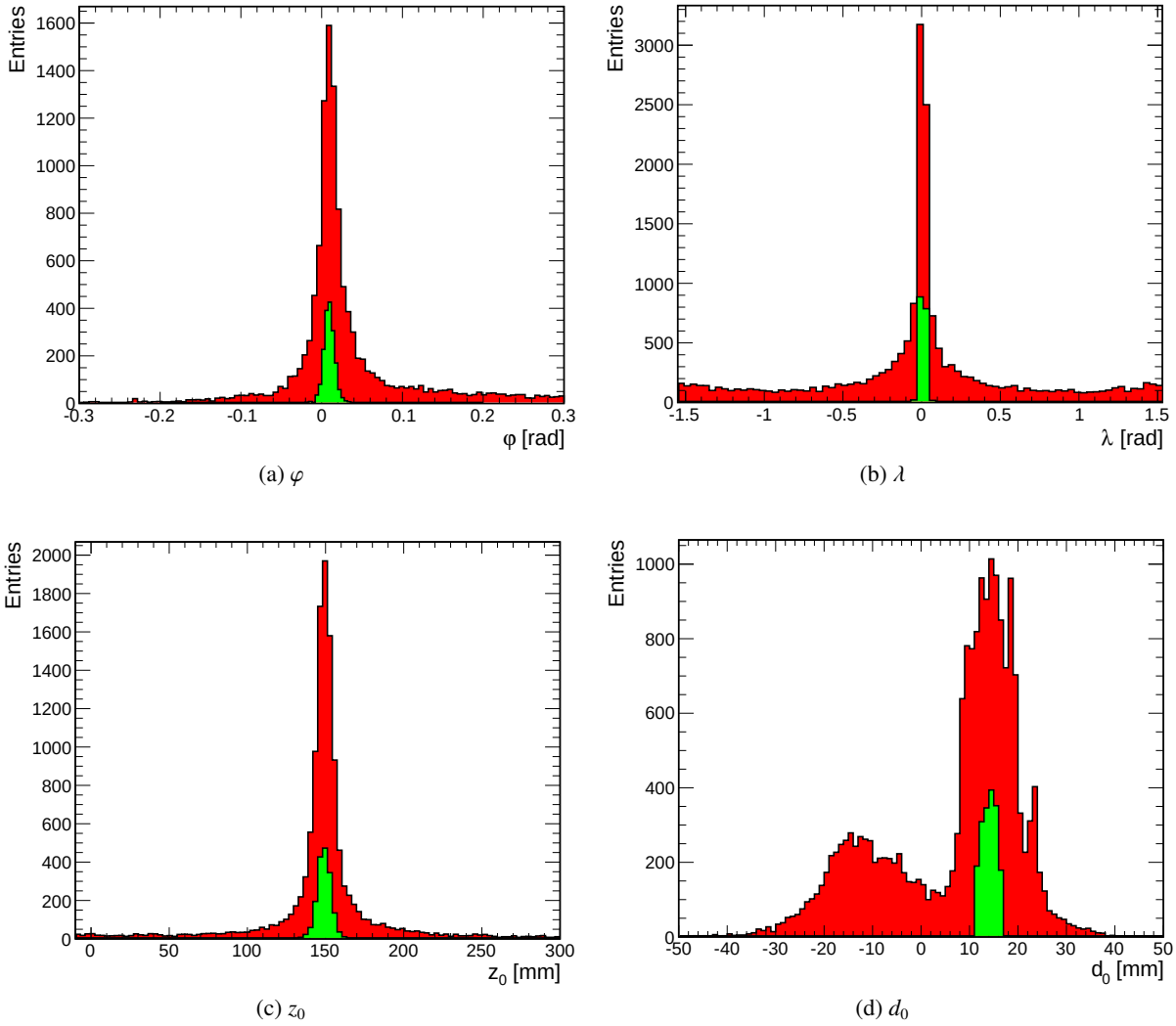


(a) $\varphi$ (b) $\lambda$

(c) $z_0$ (d) $d_0$

Figure 5.17: Track Parameters from a run with $E_{\text{Drift}} = 230\,\text{V}\,\text{cm}^{-1}$, $B = 0\,\text{T}$ and $z \approx 158\,\text{mm}$. The histograms displaying uncut data are drawn in red, while green represents the dataset remaining after cut application.

(in contrast to collider or cosmic radiation experiments), $z_0$ is not expected to be a spread-out distribution but a localized peak, spread out only due to the beam width. As most tracks are parallel to the $x$-axis of the board, $d_0$ should also be a localized peak at the center of the lower chip row. As figures 5.17c and 5.17d show, this expectation is met, for $d_0$ only after cut application. The $d_0$ distribution shows that a large fraction of tracks with extreme angles are successfully removed by the cuts from the analysed dataset.

### 5.7.4 Hit and track statistics

There are several hit and track based distributions which characterize detector performance, these are discussed in this section.

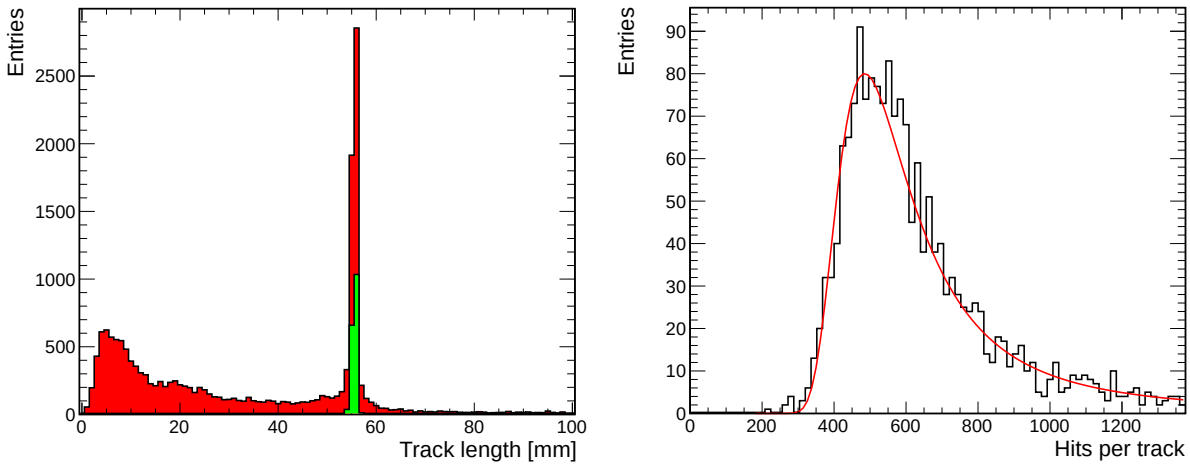


(a) Track length

(b) Hits per track. MPV: 499.9 ± 3.4

Figure 5.18: Track statistics from a run with $E_{\text{drift}} = 230\,\text{V}\,\text{cm}^{-1}$, $B = 0\,\text{T}$ and $z \approx 160\,\text{mm}$. a) The histograms are filled red, while green represents the dataset remaining after cut application. b) Landau fit on the hits per track distribution.

### Track length

The track length distribution should peak around $14\,\text{mm} \cdot 4 = 56\,\text{mm}$ if one assumes the tracks are parallel to both the readout plane and the Octoboards x-axis. As one can see in figure 5.18a this is the case. Most shorter tracks are removed by the cuts as intended, as they are most likely only partially coincide with the active detector area due to an angle substantially different from zero to the octoboard x-axis.

### Hits per track

An interesting quantity is the hits per track a detector can record, as more points per track usually result in a more accurate track reconstruction.

As every hit stems from a single primary electron, to calculate the expectation value for the hits per track it suffices to calculate the number of electron/ion pairs per centimetre $n_T$, and to extrapolate this on the length of the active area of the octoboard $l = 5.6\,\text{cm}$. $n_T$ is a constant for a given drift gas, and numerical values are taken from [56]. As the drift gas used, T2K, is a gas mixture, the resulting $n_T$ needs to be calculated from the $n_T$ of the components of T2K. According to [56] this can be done by weighted averaging. With $n_{T,\text{Ar}} = 94\,\text{cm}^{-1}$, $n_{T,\text{CF}_4} = 100\,\text{cm}^{-1}$ and $n_{T,\text{iC}_4\text{H}_{10}} = 94\,\text{cm}^{-1}$ this yields $n_{T,\text{T2K}} = 96.2\,\text{cm}^{-1}$. Extrapolating on the length of the active octoboard area this yields 538.72 hits per track, which matches the experimental results, 513 ± 3 hits per track (c.f. Fig. 5.18b) . It has to be noted, however, that 3-4 % of the data was removed while compensating for the bitshift readout system malfunction. As the bitshifts occur in all events, and the affected counts were set to zero, the number of hits in each event is reduced about 3-4 % below the real number of hits per track recorded by the module.

**Hits per track vs. z** Figure 5.19 shows the MPV of the hits per track distributions plotted versus $z$ with and without magnetic field. One expects a steep rise at low $z$. This is due to electron declustering

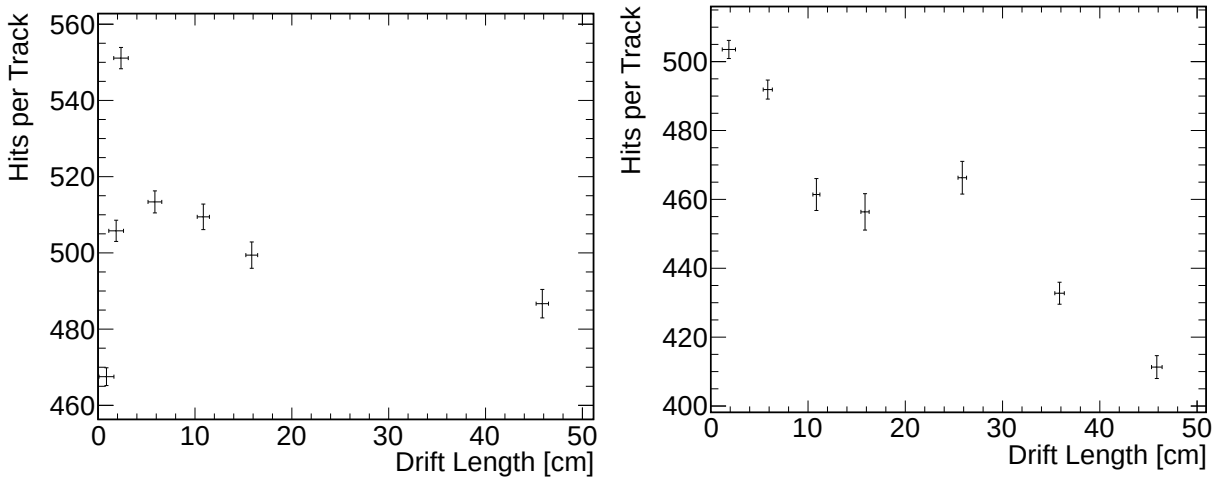


(a) z resolution $B = 0\,\mathrm{T}$

(b) z resolution $B = 1\,\mathrm{T}$

Figure 5.19: Hits per track vs $z$ for an electric field of $230\,\mathrm{V\,cm^{-1}}$.

within the gas amplification structure. Primary electrons created close to one another in the the TPC appear as a single electron if they hit the same pixel in the readout, although more charge is deposited. For larger drift distances the primary electrons will diffuse apart, increasing the chance that their avalanches won't hit the same pixel. This effect, called electron declustering, increase the number of hits per track for rising $z$. A moderate decline is expected for high $z$ due to electron attachment to electro-negative gas contaminants. With and without magnetic field the data resembles the aforementioned expectations, although the rise is not visible in the $B = 1\,\mathrm{T}$ data.

### Hits per track length

The hits per track length distribution is the same as the hits per track distribution, but normalized by the length of the track. The plotted data shows the number of hits per millimetre. This yields a more comparable number than the raw hits per track distribution. The cuts removed a lot of tracks which only partially coincide with the InGrids, which yields about 100 hits per cm, which is compatible with the expectation value calculated above, $n_{T,\mathrm{T2K}} = 96.2\,\mathrm{cm^{-1}}$.

### Hits per event

Comparing the hits per event to the hits per track distribution yields some interesting information, as the discrepancy between the MPVs of both distribution is a measure of the quality of data selection - the larger the difference the more hits in an event are not associated to a track. In an ideal case there would be zero unassociated hits. As can be seen from figures 5.20b and 5.18b the difference is negligible in our setup. The MPV for the Hits per event is $508.8 \pm 3.6$, while the MPV for the hits per track is $499.9 \pm 3.4$.

### Tracks per event

From observations during the testbeam the tracks per event distribution is expected to show mostly single tracks, some dual tracks and rapidly diminishing numbers of higher track multiplicity. As figure 5.13c shows this is exactly what the analysis yields.

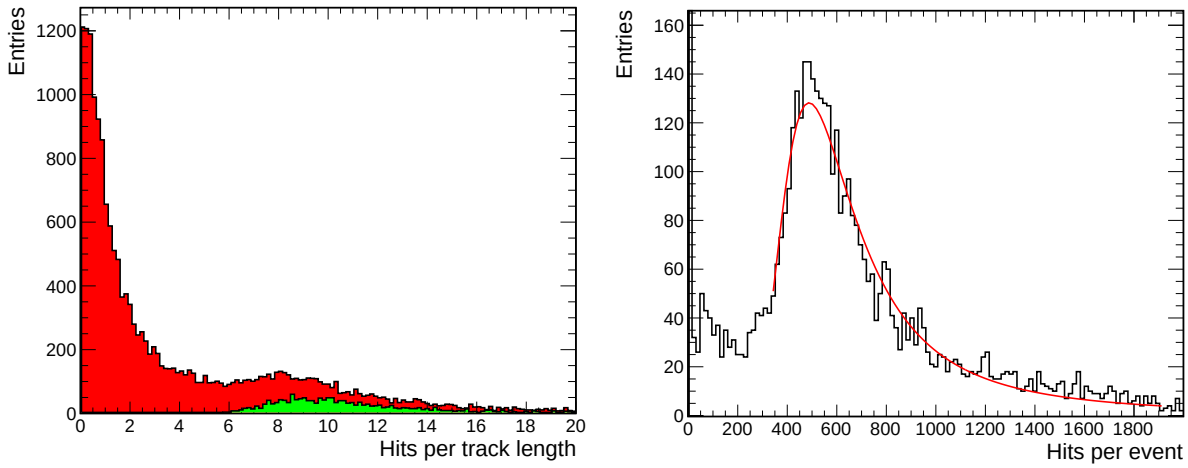


(a) Hits per tracklength

(b) Hits per event. MPV: 508.8 ± 3.6

Figure 5.20: Track statistics from a run with $E_{\text{Drift}} = 230\,\text{V}\,\text{cm}^{-1}$, $B = 0\,\text{T}$ and $z \approx 160\,\text{mm}$. The uncut histograms are filled red, while green represents the dataset remaining after cut application.

### 5.7.5 Spatial resolution

To determine the resolution of the detector, first the residuals were calculated.

#### Residuals

Residuals are the distances of hits from their associated tracks. Results for $xy$ and $z$ residual distributions integrated over $x$ are shown in figure 5.21. The mean value of this distribution is zero if the track fit was successful. The RMS of the distribution is a measure for the detectors single point resolution $\sigma_N$. For the $xy$ residuals, the distribution peaks around zero, while this in not the case for the $z$ residuals. The asymmetry causing this is introduced by the timewalk effect.

#### $xy$ residuals versus $x$

Histograms like the one presented in figure 5.21a were made for thin slices of about 10 pixels in the direction of the beam ($x$). These were all added to the same 2D-histogramm, and are shown color-coded in figure 5.22. The histograms shown in the figure are derived from data from a run with $z \approx 110\,\text{mm}$. Here one can observe two striking features:

- One can observe the distribution is much sharper for an active magnetic field, this is due to the reduced diffusion.
- Especially in the case of $B = 1\,\text{T}$, one observes a tilt in the distribution for the central chips.

Field inhomogeneities and $\vec{E}\times\vec{B}$-effects may be the reason for the tilt. In order to investigate this further, the plots shown in figure 5.22 were decompiled into the individual $x$-slices, and the mean and RMS were calculated independently. It is expected that the RMS is a measure for the diffusion contribution, while the shift of the mean is caused by field effects. If the shift in the mean is really caused by field distortions, the field simulations shown in figure 5.4 suggest that the deviation of the mean should be minimal at the centre, while it should be maximal at the edges of the chips. Both mean and RMS were plotted versus

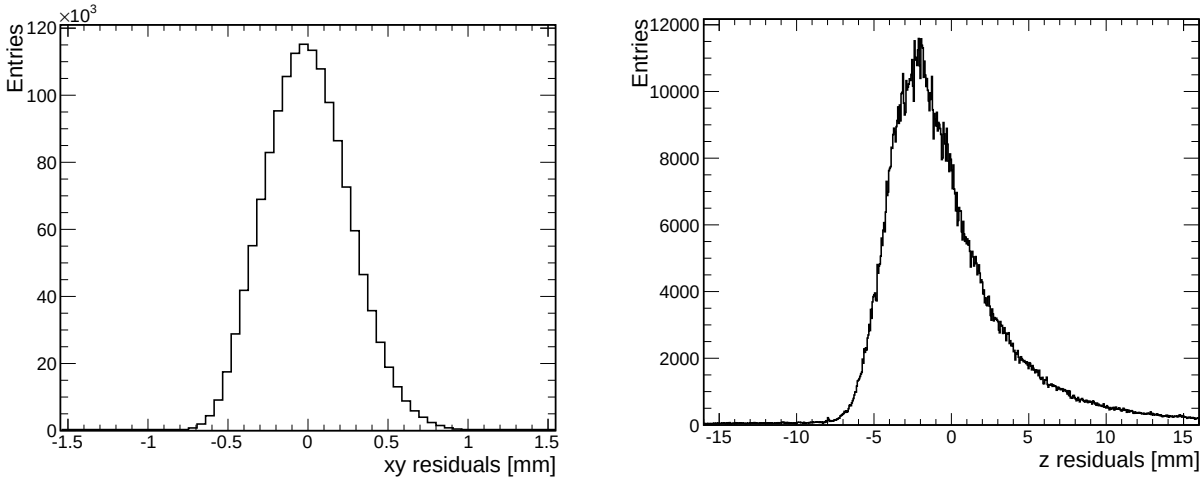


(a) *xy* residuals (b) *z* residuals

Figure 5.21: *xy* and *z* residuals obtained from a run with $E_{\text{Drift}} = 230\,\text{V}\,\text{cm}^{-1}$, $B = 0\,\text{T}$ and $z = 58.8\,\text{mm}$.

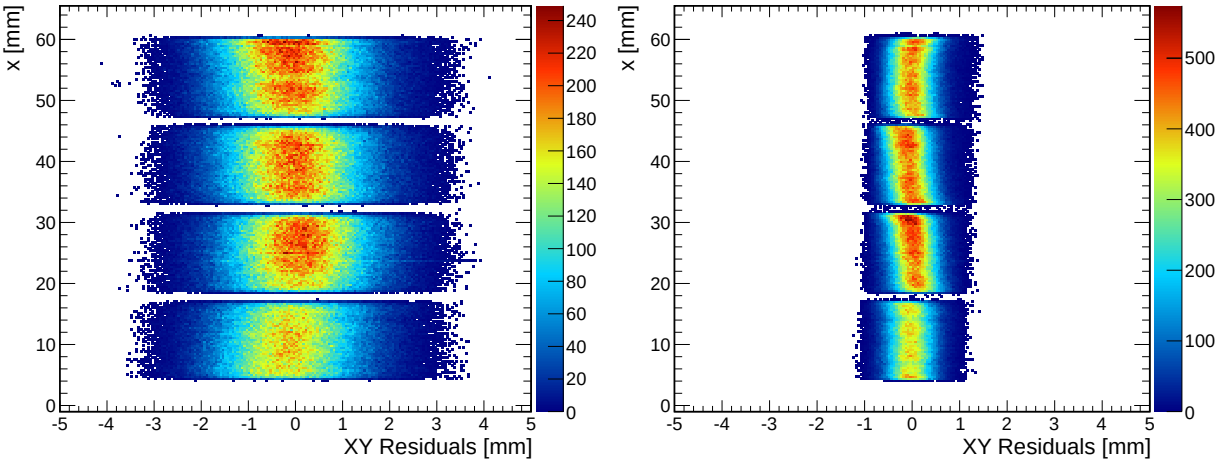


(a) $B = 0\,\text{T}$ (b) $B = 1\,\text{T}$

Figure 5.22: xy residuals vs x at $z \approx 110\,\text{mm}$, with and without magnetic field.

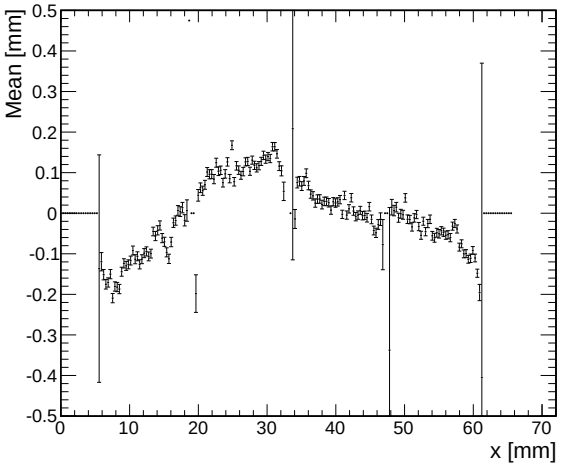


(a) Mean,$z \approx 110\,\text{mm}$, $B = 0\,\text{T}$

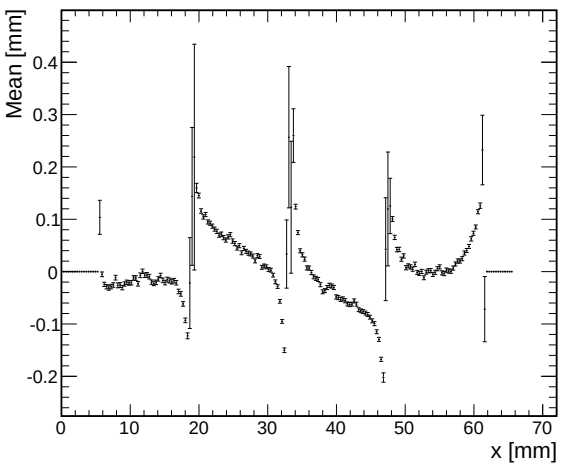


(b) Mean,$z \approx 110\,\text{mm}$, $B = 1\,\text{T}$

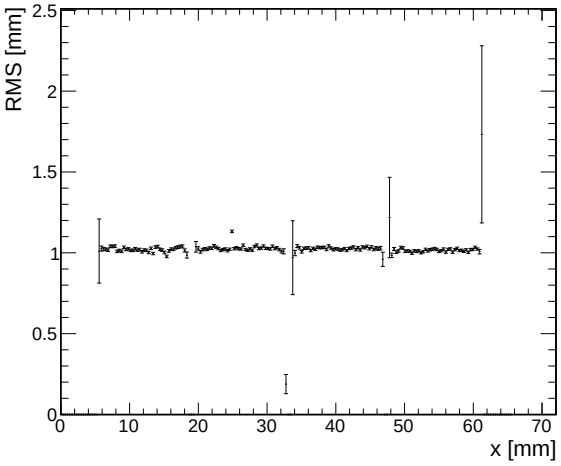


(c) RMS,$z \approx 110\,\text{mm}$, $B = 0\,\text{T}$

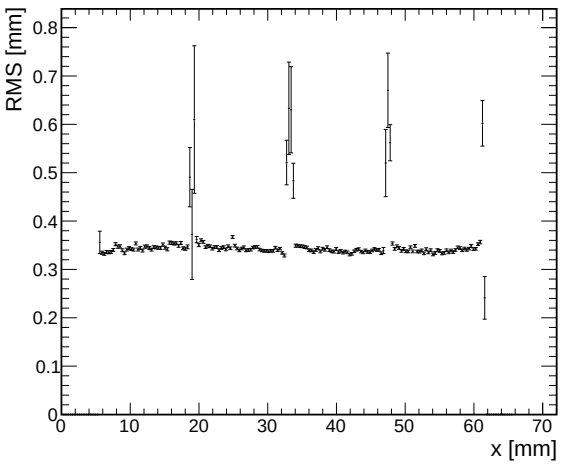


(d) RMS,$z \approx 110\,\text{mm}$, $B = 1\,\text{T}$

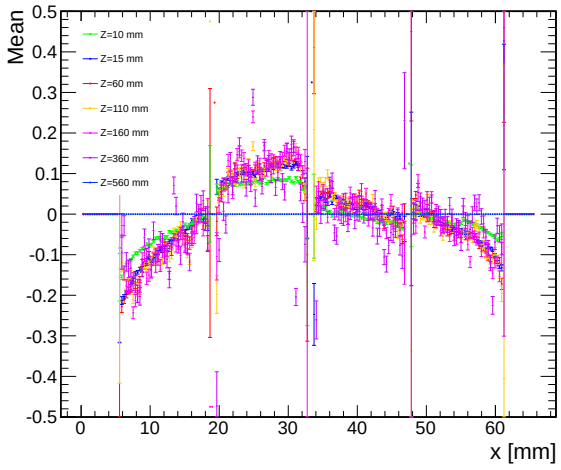


(e) Mean, all z, $B = 0\,\text{T}$

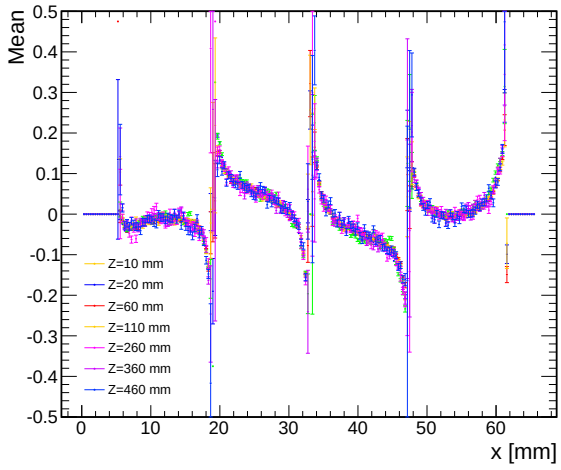


(f) Mean, all z, $B = 1\,\text{T}$

Figure 5.23: Mean and RMS of the xy residuals (c.f. figure 5.22 for different values of x, with and without magnetic field.

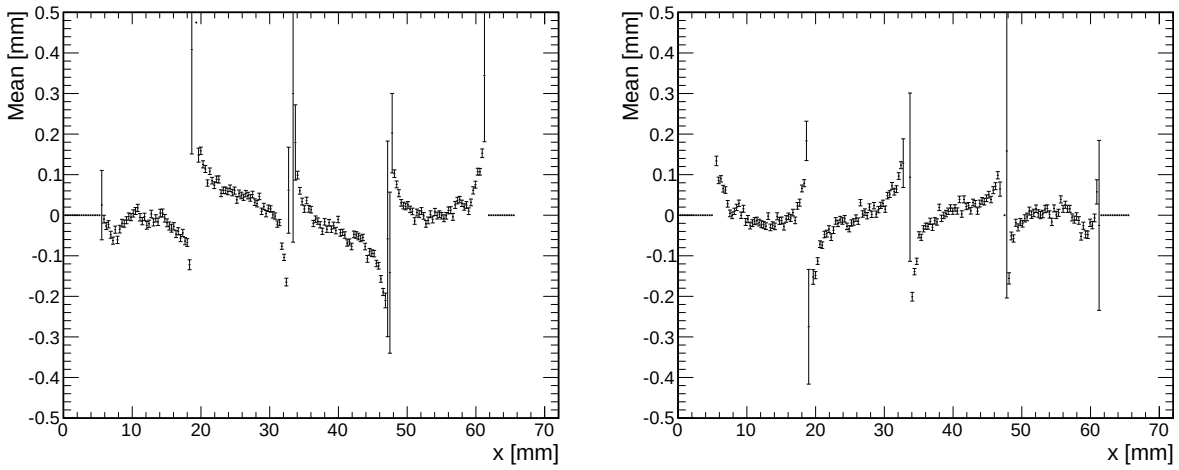


(a) Mean,$z \approx 210$ mm, original

(b) Mean,$z \approx 210$ mm, mirrored

Figure 5.24: Mean of the xy residuals for different values of x, with magnetic field. a): The original distribution. b): The mirrored distribution, showing the same features.

$x$, results are presented in figure 5.23. From the distributions of the means one can deduce that the field effects really are the major reason for the tilt of the distribution, as while the deviations from zero are about the same in both cases (around 0.2 mm), the B=0 T plot is much smoother and more continuous. The fact that the deviation from zero is point-symmetric for active magnetic field is probably due to $\vec{E} \times \vec{B}$-effects. From the field distortions alone one would expect, keeping in mind the simulation results presented in figure 5.4, reflection-symmetric deviations.

According to equation 2.14 the RMS for B=0 T should be 1032 µm (with $z \approx 110$ mm and $D_T = 311.3\,\mu\text{m}/\sqrt{\text{cm}}$ as simulated with Magboltz), as one can see in figure 5.23c, the measured value is $1022 \pm 16$ µm. For B=1 T the RMS is expected to be 312 µm (with $z \approx 110$ mm and $D_T = 94.1\,\mu\text{m}/\sqrt{\text{cm}}$ according to Magboltz simulations), the measured value is $312 \pm 6$ µm according to figure 5.23d. This was examined further by comparison of the deviations of the means of the $xy$-residuals distributions from zero for multiple values of $z$. One observes that the distributions agree with each other, confirming the structure is caused by E-field inhomogeneities between the InGrids.

It was speculated that the difference between the signal on the left and right chips could be due to a biased analysis, as the origin is not in the centre of the distribution (it is in fact on the lower left corner of the Octoboard). To verify this, a mirrored dataset was created by swapping columns in each raw datafile individually and modifying the GEAR file accordingly. This new dataset was then analysed again (c.f. figure 5.24), yielding the same structure, but mirrored - this rules out any bias introduced by the analysis.

With this excellent agreement of experiment and expectation, the assumption, that the broadening of the distribution stems from diffusion, while the tilt is caused by field inhomogeneities, and from $\vec{E} \times \vec{B}$-effects in the case of active magnetic field, in the vicinity of the grid, seems reasonable.

### Field distortion correction

It is assumed that the tilt observed in the $xy$ residuals vs. $x$ distribution broadens the residuals distributions and, thus, degrades the detectors resolution, since the tilt is observed on each chip independently, which is why it probably interferes with a proper track fit.

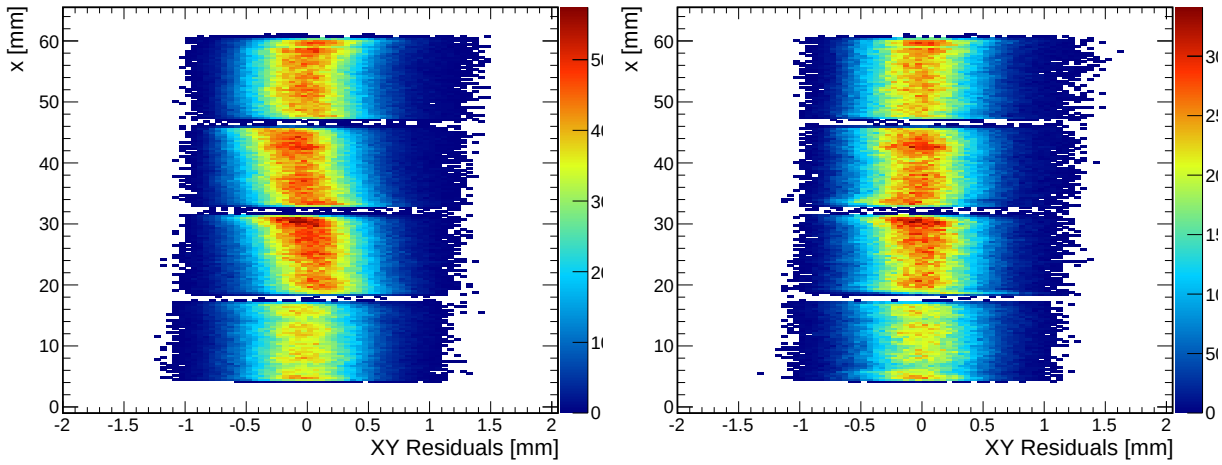


(a) Original (b) Corrected

Figure 5.25: xy residuals vs z. a): Zoom-in of figure 5.22b. b): Mean-corrected distribution.

Thus, an attempt to correct the field distortions was made. During the correction, hits are shifted along the $y$-axis of the Octoboard using the mean for a given $x$-bin of all distributions shown in figure 5.23f as offset. Results are presented in figure 5.25. The correction appears successful, although there remain some distorted features especially between the two chips in the center. This was investigated further, by again considering the mean deviations of the residual distributions from zero, leading to the results presented in figure 5.26a.

While the distribution looks more ordered, the deviations from zero are still in the order of magnitude of 100 µm. It seems some points were "over-corrected". It is suspected that the reason for this is an asymmetry, which occurs in $xy$-residuals distributions for $x$-values close to a chip boundary. Thus, it was theorized, that an iterative approach might be more successful. The means before and after the first correction were added for the second iteration. Results of this new iteration are presented in figure 5.26b. As one can clearly see, this procedure also did not have the desired effect.

### Single point resolution

The single point resolution can be calculated from the RMS of the $xy$- and $z$-residuals distributions shown in figure 5.21. It is, however, biased, as it takes all points of the track into account, even the one which is currently looked at, resulting in a value which is systematically too small. For compensation, the geometric mean of $\sigma_N$ and $\sigma_{N-1}$ is calculated, where the latter takes all points into account except the one which is currently looked at. As discussed in [55], [57] this is a correct expression for the single point resolution, which then becomes

$$\sigma_{\text{geo}} = \sqrt{\sigma_N \sigma_{N-1}}. \tag{5.11}$$

This now corresponds to the expressions from equations 2.14. These resolutions, $\sigma_{\text{geo}\,xy}$ and $\sigma_{\text{geo}\,z}$ respectively, can also be plotted versus $z$. In both cases one would naively assume the distribution resembles the single electron diffusion limit.

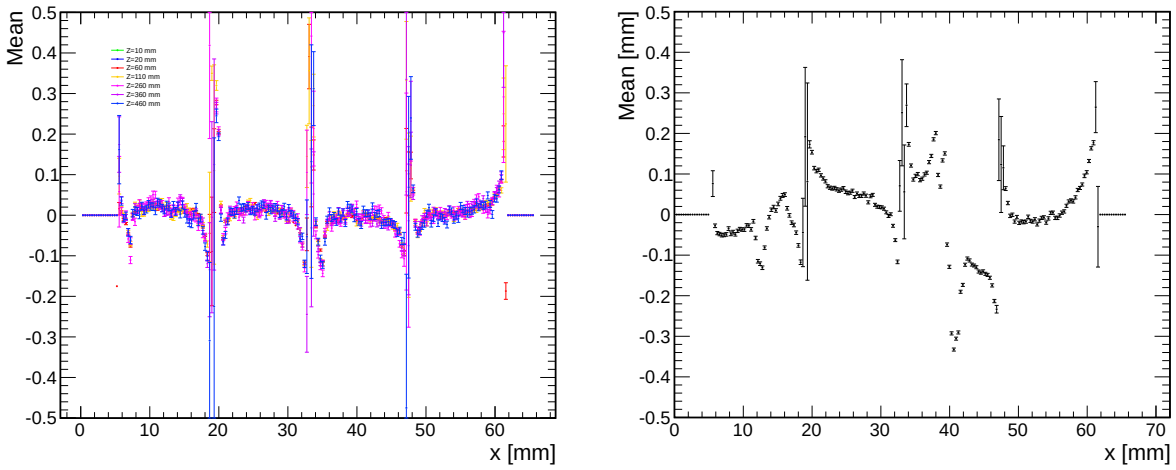


(a) Mean, all z, $B = 1\,\mathrm{T}$, after first correction.

(b) Mean, $z = 110\,\mathrm{mm}$, $B = 1\,\mathrm{T}$, after second correction.

Figure 5.26: $xy$-residuals mean, $B = 1\,\mathrm{T}$, after correction.

**Field distortion correction effects** The field distortion correction has negligible influence on the single point resolution, as can be seen from the comparison of figures 5.28b, 5.27a and figures 5.29b, 5.27b, respectively. This is not surprising, since as discussed above, the width of the $xy$-residuals mean distribution was still in the order of magnitude of 100 µm after the correction.

**Transverse resolution** In the case of $\sigma_{\mathrm{geo}\,xy}$ the experimental results follow the single electron diffusion limit as expected, as figure 5.28 shows. The transverse diffusion $D_T$ should drop by a factor of three if a magnetic field is applied (for $B = 1\,\mathrm{T}$, $E_{\mathrm{drift}} = 230\,\mathrm{V\,cm^{-1}}$), as according to Magboltz simulations it drops from 311.3 µm/ $\sqrt{\mathrm{cm}}$ to 94.1 µm/ $\sqrt{\mathrm{cm}}$. This is resembled in the experimental data, here $D_T$ drops from (313 ± 4) µm/ $\sqrt{\mathrm{cm}}$ to (99 ± 1) µm/ $\sqrt{\mathrm{cm}}$. The simulated and measured values are also compatible.

The intrinsic detector resolution $\sigma_{xy,0}$, given by the $y$-intercept in figure 5.28, is expected to be:

$$\sigma_{0,xy} = \frac{55\,\mu\mathrm{m}}{\sqrt{12}} = 15.9\,\mu\mathrm{m}, \tag{5.12}$$

due to the pixel pitch on a Timepix chip of 55 µm. The factor of $\frac{1}{\sqrt{12}}$ enters due to the binning in terms of the pixels [58]. Further, the intrinsic resolution should be the same with and without magnetic field, if one assumes the magnetic field only reduces the diffusion. If one however considers $E \times B$ effects, one would expect $\sigma_{xy,0}$ to change if a magnetic field is applied. Further, one would expect $\sigma_{xy,0}$ to drop if a magnetic field is active, as due to their low mass, electrons rather follow magnetic field lines than electric ones according to equation 2.3. As electric field distortions (e.g. at the grid boundaries) degrade the resolution, the addition of an magnetic field would homogenize the electrons drift trajectories, thus improving $\sigma_{xy,0}$. This assumption is verified by the experimental data, since if a magnetic field is activated $\sigma_{xy,0}$ indeed drops from (238 ± 81) µm to (141 ± 13) µm. The deviation from the expectation from equation 5.12 is most likely due to uncorrected field distortions.

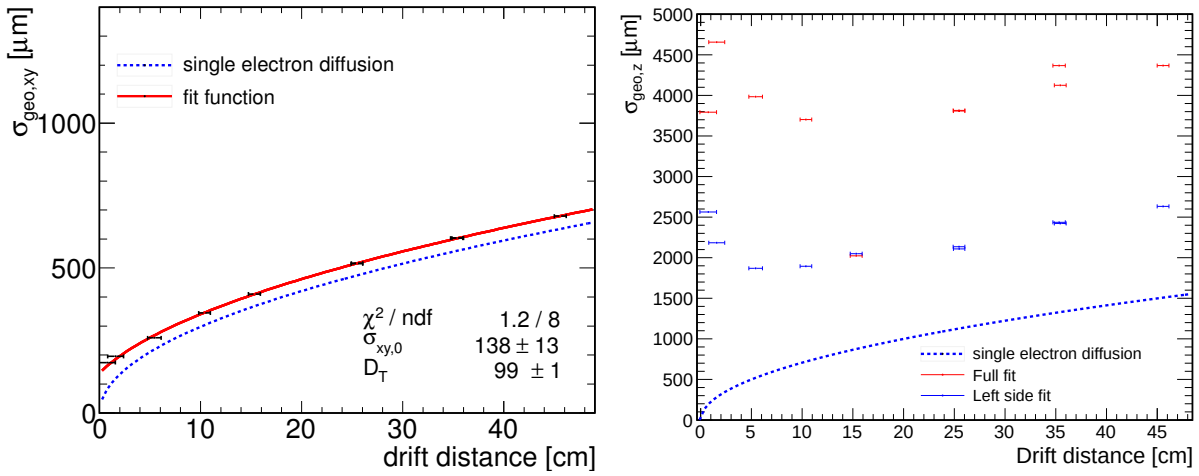


(a) Corrected tansverse resolution $B = 1\,\mathrm{T}$ (b) Corrected longitudinal resolution $B = 1\,\mathrm{T}$

Figure 5.27: Field-distortion corrected transverse and longitudinal resolution obtained from runs with $E_{\mathrm{Drift}} = 230\,\mathrm{V\,cm^{-1}}$, and $B = 0\,\mathrm{T}$ and $B = 1\,\mathrm{T}$.

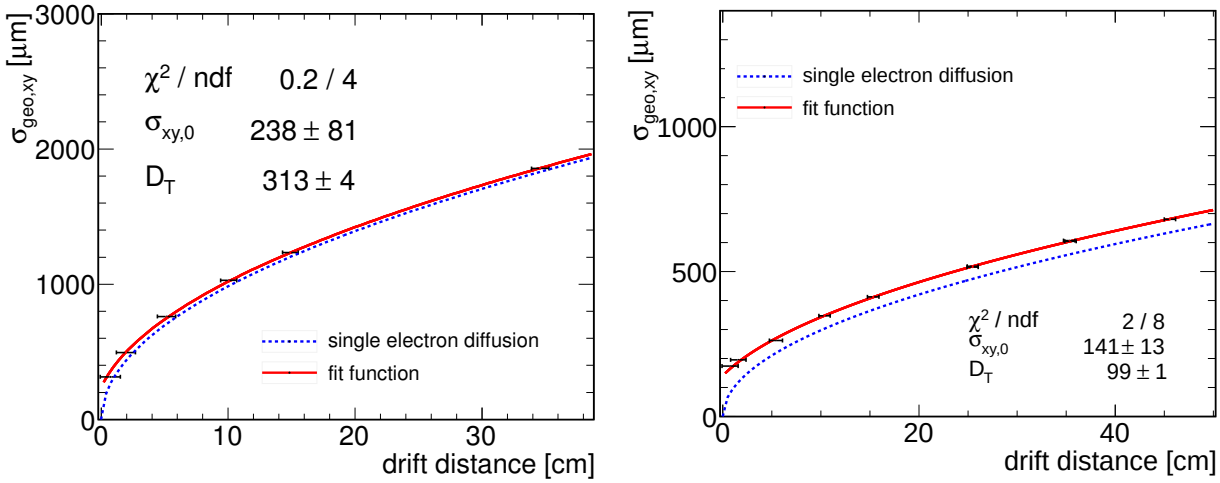


(a) xy resolution $B = 0\,\mathrm{T}$ (b) xy resolution $B = 1\,\mathrm{T}$

Figure 5.28: Transverse resolution obtained from runs with $E_{\mathrm{Drift}} = 230\,\mathrm{V\,cm^{-1}}$, and $B = 0\,\mathrm{T}$ and $B = 1\,\mathrm{T}$.

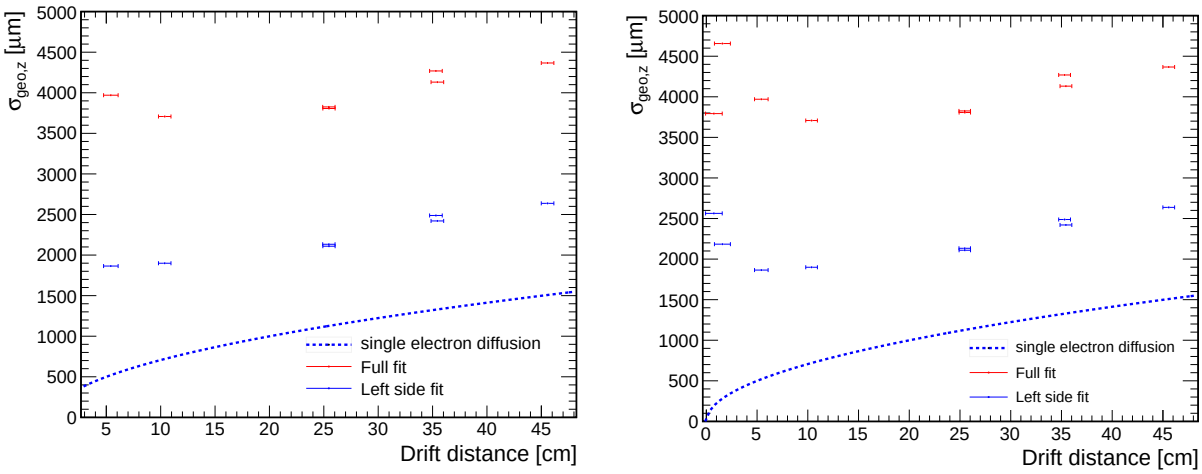


(a) z resolution $B = 0\,\mathrm{T}$

(b) z resolution $B = 1\,\mathrm{T}$

Figure 5.29: Longitudinal resolution obtained from runs with $E_{\mathrm{Drift}} = 230\,\mathrm{V\,cm^{-1}}$, and $B = 0\,\mathrm{T}$ and $B = 1\,\mathrm{T}$.

**Longitudinal resolution** In the ideal case, the longitudinal resolution would follow the single electron diffusion just like the transverse resolution does. However, as can be seen in figure 5.29, this is not the case. The resolution is much worse than the theoretical limit. This has two major reasons. One is the readout frequency of $f_c = \frac{1}{T_c} = 40\,\mathrm{MHz}$, which imposes a much harder limit to the resolution than the diffusion does. From equation 5.2 it follows that the error on the drift time is

$$\Delta t_d = \sqrt{\Delta t^2_{\mathrm{Shutter}} + \Delta\left(\frac{n}{f_{\mathrm{clock}}}\right)^2}. \tag{5.13}$$

Both the shutter time and the count value have an error of one clock cycle, since this is the quantization error due to the clock. According to [58] a factor of $\frac{1}{\sqrt{12}}$ enters due to the binning in terms of clock cycles. Thus, $\Delta t_d$ reads [15]:

$$\Delta t_d = \sqrt{\frac{2T_c^2}{12}}. \tag{5.14}$$

To calculate the limit which the readout frequency poses for the longitudinal resolution, the above expression is converted to a length by multiplying with the drift velocity $v_d$:

$$\sigma_{z,ro} = \frac{T_c v_d}{\sqrt{6}}. \tag{5.15}$$

This yields $\sigma_{z,ro} = (755.2 \pm 0.5)\,\mu\mathrm{m}$ for $E_{\mathrm{Drift}}$=230 $\mathrm{V\,cm^{-1}}$.

Timewalk, however, is the dominating effect. Timewalk is the amount of clock cycles counted too less due to threshold effects, which results in too long drift times. The timewalk is up to several 10 clock cycles, which according to

$$\sigma_{z,tw} = v_d \cdot t_c \tag{5.16}$$

would yield $\sigma_{z,tw} \approx 3700\,\mu\mathrm{m}$ for a timewalk of 20 clock cycles, which together with the readout frequency effect easily explains the large value for $\sigma_{z,0}$.

The timewalk was corrected for in figure 5.29. For the transverse resolution, as well as the red points

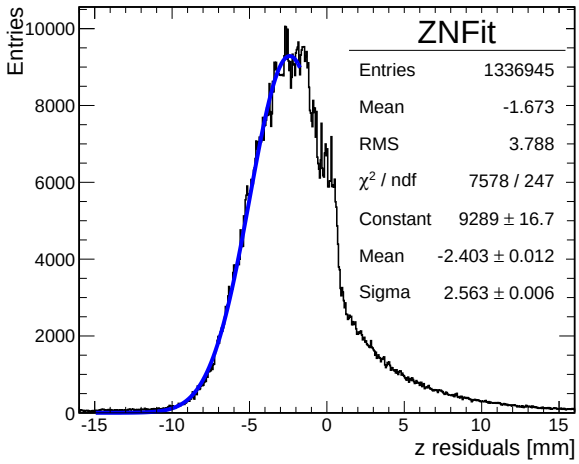


Figure 5.30: z residuals at $z = 10\,\text{mm}$. The blue curve represents the timewalk correction.

in figures 5.29a and 5.29b, the RMS of the whole peak shown in figure 5.21 was computed. To correct for the timewalk effect, instead a fit was applied only to the leading edge of the peak shown in figure 5.30. As one can see in this example, by correcting for the timewalk, $\sigma_z$ drops from about 3790 µm to 2570 µm. Timewalk-corrected results are marked in blue in figure 5.29a. As can be seen, the blue points are approximately 1000 µm above the single electron diffusion limit, compatible with the readout limit of $(755.2 \pm 0.5)$ µm.

# Chapter 6

# Conclusion

The future International Linear Collider will feature two detectors, one of them is the International Large Detector (ILD). The ILD will feature a Time Projection Chamber (TPC) as a tracker. For research and development purposes, a prototype of this TPC was built at DESY by the LC-TPC collaboration. It is called the Large Prototype (LP). Both the prototype, and the ILD TPC, feature a modular readout. In preparation for a future full area module, within this thesis two LP modules, one using GEMs for gas amplification, the other InGrids, were designed, built and tested. Both modules carry an eight-chip Timepix board. The modules were designed in such a way, that methods and design considerations, relevant to the future 100-chip module, could be tested.

First some basic Timepix temperature related experiments were conducted. It was established that a PCB, hosting Timepix chips, should have about 15 vias per $(1.4\,\mathrm{cm})^2$ for optimal thermal conductance, and heat dissipation, respectively. This was considered during the design of the two Ocotoboard modules for the LCTPC Large Prototype at DESY. Both modules were designed with a water cooling system, and the cooling unit carrying all the module electronics was designed to be removable even if the module is installed at the LP. The cooling system was successfully tested.

During the testbeam at the test array T/24 at DESY II, both modules were installed in the LP. They performed within the design goals and over one million events were recorded.

During the initial analysis, basic properties of the detector, like gas gain and drift velocities, were obtained from the data. Both matched the expectations, proving the detector is understood. An occupancy map of the full module was created using high statistics, to asses the beam position and each chips performance - all as expected.

After data cleaning, a strict set of selection rules was applied to the dataset to filter out straight, fully recorded tracks. This was done in order to allow for a fast progressing analysis, delivering results on the key characteristics of the modules. The effects of the cuts were carefully studied. It was established the cuts had the desired effect.

The main benchmark for the module, the transverse single point resolution, was computed to $\sigma_{xy,0} = (140 \pm 14)\,\mu\mathrm{m}$. It follows the single electron diffusion limit, as expected. The deviation of the longitudinal single point resolution from the single electron diffusion limit was fully understood. It stems from the timewalk effect, which was corrected for, and limits in the current version of the readout system.

The analysis of the data taken with the InGrid module proved this type of readout is an ideal candidate for a future linear collider TPC. With more than 90 hits per centimetre an InGrid based readout really makes the most convincing feature of a TPC, the huge number of track points, excel over other types of trackers.

Summing up, during this thesis two detector modules were developed, built and tested. The successful test of a large area InGrid based detector with more than 520k pixels on its own is a great accomplishment, paving the way for the future 100 chip module.

# Appendix A

# Useful information

## A.1 Bit to count lookup-table

| Count | bit pattern |
|---|---|
| 425 | 11110000100010 |
| 393 | 11110000110010 |
| 343 | 11110001100010 |
| 585 | 11110010000011 |
| 447 | 11110011000000 |
| 322 | 11110100000100 |
| 491 | 11110101010110 |
| 485 | 11110111110101 |
| 373 | 11111000001000 |
| 424 | 11111000010001 |
| 392 | 11111000011001 |
| 342 | 11111000110001 |
| 490 | 11111010101011 |
| 484 | 11111011111010 |
| 423 | 11111100001000 |
| 391 | 11111100001100 |
| 341 | 11111100011000 |
| 483 | 11111101111101 |
| 482 | 11111110111110 |
| 481 | 11111111011111 |

Table A.1: Excerpt from the lookup table used to translate the bit patterns of the pixels counter to count values. The last entry is a candidate for bit-shifts, as it has only one zero.

## A.2 MarlinTPC Processors

During the analysis described in chapter 5, several MarlinTPC processors were used. In the following all processors and their functionality will be described.

### A.2.1 General processors

**AIDAProcessor** The AIDA processor is responsible for organizing and creating histograms. It has to be called in any steering file.

**LCIOOutputProcessor** This processor writes all transient collections into a specified LCIO output file.

**TimePixMapHandlerProcessor** Different maps are needed during the analysis, e.g. status and mode maps, defining which pixels are operational and which mode they are configured to. This processor makes the maps available to other processors.

### A.2.2 Data read-in and calibration

**OctoboardReaderProcessor** A modification of the TimePixReaderProcessor, this processor was written to allow for the read-in of multi chip data. It also cleans the data from the readout system artefacts described in section 5.6.1.

**TimePixZeroSuppresionProcessor** This processor performs zero suppression. In case of the LCIO data format, non-zero suppressed data is stored in vectors, were the position within the vector identifies the pixel. Usually most of the entries in a vector are zero, such that the data files are unnecessarily large. The zero suppression algorithm now changes the data structure such that a vector begins once a pixel has non-zero output, with its first entry being that pixels ID and the following entry being the ADC value of the pixel. If the next pixel also has non-zero output, its ADC value is simply added as the next entry in the vector and so on, until a pixel wasn't activated, which is when the vector ends. A new vector is created once another pixel is activated.

**TrackerRawDataToDataConverterProcessor** This processor transforms the data from one format into another.

**TimePixCalibrationProcessor** This processor applies the calibration on the data, and needs a calibration map as input. In the case of an InGrid based detector, this is only necessary for ToT data. Here the ADC counts are transformed to electrical charge.

**OctoboardHitAndTrackChargeProcessor** The OctoboardHitAndTrackChargeProcessor is used to extract the Polya distributions for each chip individually.

### A.2.3 Reconstruction

**InGridSimpleClusterFinder** For most MPGD readouts, e.g. GEMs, hits form clusters, as the avalanche developing in a GEM will hit multiple (neighbouring) pixels - such a charge deposition over multiple pixels is then called a cluster. For InGrids this is not the case, nevertheless, in order to be able to use the MarlinTPC-chain, a conversion of hits to clusters is needed. This is performed in this processor.

**TrackFinderHoughTrafoProcessor** This processor does the assignment of hits to tracks by means of a Hough transformation. It makes collections of track candidates available to the subsequent analysis.

**LinearRegressionProcessor** The LinearRegressionProcessor calculates the track parameters of the track candidate collections provided by the TrackFinderHoughTrafoProcessor by a linear regression.

### A.2.4 Analysis

**TimePixOccupancyProcessor** This processor computes the occupancy of a Timepix chip. It was modified to allow for multiple chips, however, there is a histogram created for each chip.

**CutApplicationProcessor** This processor can apply various pre-defined cuts on the data, special cuts considering the Octoboard geometry have been added.

**LinearGeometricMeanResolutionProcessor** This processor calculates unbiased residuals according to equation 5.11.

**XYZDistributionTracksProcessor** The XYZDistributionTracksProcessor calculates x,y,z and x vs y track distributions.

**TrackParametersDistributionProcessor** This processor calculates the $\lambda$, $\varphi$, $d_0$ and $z_0$ distributions.

**HitAndTrackCounterProcessor** This processor calculates various hit and track statistics, including hits per event and tracks per event. It was expanded to also provide a tracklength histogramm.

### A.2.5 Miscellaneous

**OctoboardCorrectionProcessor** To apply the field distortion corrections discussed in section 5.7.5.

# Bibliography


[1] G. Aad et al., 'Observation of a new particle in the search for the Standard Model Higgs boson with the ATLAS detector at the LHC', *Physics Letters B* (2012).

[2] S. Chatrchyan et al.,
'Observation of a new boson at a mass of 125 GeV with the CMS experiment at the LHC', *Physics Letters B* (2012).

[3] S. Catani et al., 'QCD' (2000), eprint: hep-ph/0005025.

[4] A. Vogel, 'Beam-Induced Backgrounds in Detectors at the ILC', 2008.

[5] K. Desch and P. Bechtle, *Collider Physics*, Lecture at University of Bonn, 2013.

[6] R. Heuer et al., 'TESLA Technical Design Report Part III: Physics at an e+e- Linear Collider' (2001).

[7] ILD Concept Group, *International Large Detector DBD*,
URL: http://ilcild.org/documents.

[8] T. Behnke et al., *ILC Technical Design Report*, 2013.

[9] ILC Global Design Effort, *ILC conceptual diagram*,
URL: http://www.linearcollider.org/images/.

[10] ILD Collaboration, *ILD Detector Systems*,
URL: http://ilcild.org/ild-detector-systems.

[11] M. Lupberger, private communication.

[12] W. Blum, W. Riegler and L. Rolandi, *Particle Detection with Drift Chambers*,
Particle acceleration and detection, Springer, 2008, ISBN: 9783540766841.

[13] P. Langevin, 'Sur la Theorie du Mouvement Brownien',
*C. R. Acad. Sci. Paris* 146 (1908) 530–533.

[14] D. S. Lemons and A. Gythiel,
'Paul Langevin's 1908 paper "On the Theory of Brownian Motion" ["Sur la theorie du mouvement brownien," C. R. Acad. Sci. (Paris) [146], 530–533 (1908)]',
*American Journal of Physics* 65.11 (1997) 1079–1081, DOI: 10.1119/1.18725,
URL: http://link.aip.org/link/?AJP/65/1079/1.

[15] C. Brezina, *A GEM based time projection chamber with pixel readout*, MBV Berlin, 2013,
ISBN: 9783863873301.

[16] H. Hilke, 'Time projection chambers', *Rept.Prog.Phys.* 73 (2010) 116201,
DOI: 10.1088/0034-4885/73/11/116201.

[17] S. Amendolia et al.,
'Dependence of the transverse diffusion of drifting electrons on magnetic field',
*NIM-A* 244.3 (1986) 516 –520, ISSN: 0168-9002,
DOI: http://dx.doi.org/10.1016/0168-9002(86)91077-6.

[18] A Buzulutskov et al.,
'First results from cryogenic avalanche detectors based on gas electron multipliers',
*IEEE TNS* 50.6 (2003) 2491–2493.

[19] S. Lotze, 'Ion backdrift minimisation in a GEM-based TPC readout',
PhD thesis, Universitätsbibliothek, 2006.

[20] C. Krieger, *Messung von Transferkoeffizienten einer GEM-Auslesestruktur*, 2009.

[21] R. Menzen, 'Charakterisierung von GEMs', 2010.

[22] F. Sauli, 'GEM: A new concept for electron amplification in gas detectors',
*NIM-A* 386.2 (1997) 531–534.

[23] Y. Giomataris et al., 'MICROMEGAS: a high-granularity position-sensitive gaseous detector for high particle-flux environments', *Nuclear Instruments and Methods in Physics Research Section A: Accelerators, Spectrometers, Detectors and Associated Equipment* 376.1 (1996) 29–35.

[24] A Delbart et al., 'New developments of Micromegas detector',
*Nuclear Instruments and Methods in Physics Research Section A: Accelerators, Spectrometers, Detectors and Associated Equipment* 461.1 (2001) 84–87.

[25] S. G. Kappler, 'Higgs Search Studies in the Channel $t\bar{t}H$ with the CMS Detector at the LHC and Development of a GEM-based TPC Readout for Future Collider Experiments' (2004).

[26] V. B. Carballo et al.,
'A radiation imaging detector made by postprocessing a standard CMOS chip',
*Electron Device Letters, IEEE* 29.6 (2008) 585–587.

[27] X. Llopart et al., 'Medipix2: A 64-k pixel readout chip with 55- mu;m square elements working in single photon counting mode', *IEEE TNS* 49.5 (2002) 2279–2283, ISSN: 0018-9499,
DOI: 10.1109/TNS.2002.803788.

[28] X. Llopart et al., 'Timepix, a 65k programmable pixel readout chip for arrival time, energy and/or photon counting measurements', *NIM-A* 581.1 (2007) 485–494.

[29] M Chefdeville et al.,
'An electron-multiplying Micromegas grid made in silicon wafer post-processing technology',
*NIM-A* 556.2 (2006) 490–494.

[30] H. van der Graaf,
'GridPix: An integrated readout system for gaseous detectors with a pixel chip as anode',
*NIM-A* 580.2 (2007) 1023–1026.

[31] Y Bilevych et al., 'Spark protection layers for CMOS pixel anode chips in MPGDs',
*NIM-A* 629.1 (2011) 66–73.

[32] W. Demtröder, *Experimentalphysik 1: Mechanik und Wärme*, Experimentalphysik,
Springer London, 2008, ISBN: 9783540792956.

[33] Rüdiger Paschotta, *Wärmewiderstand*, URL: enlex.info.

[34] M. Lenz, G. Striedl and U. Fröhler, *Thermal Resistance, Theory and Practice*,
Infineon Technologies AG, Munich, Germany, 2000.

[35] DESY, *Test Beams at DESY - beam generation*, URL: http://testbeam.desy.de/e130573.

[36] K. Dehmelt, 'The large TPC prototype for an ILC detector', *IEEE NSSCR/MIC*, IEEE, 2008 3388–3390.

[37] M. Lupberger, 'Towards large scale pixelated gaseous detectors', MPGD2013, Zaragoza, 2013.

[38] T. Behnke et al., 'A lightweight field cage for a large TPC prototype for the ILC', *JInst* 5.10 (2010) P10011.

[39] J Alozy et al., 'First Version of the PCMAG Field Map', *EUDET-Memo-2007-51* (2007).

[40] J. Ottnad, private communication, 2013.

[41] Jarkko Brennecke, Q-print electronic GmbH, private communication, 2013.

[42] D. Lide, *CRC Handbook of Chemistry and Physics: A Ready-reference Book of Chemical and Physical Data*, CRC Handbook of Chemistry and Physics, 85th Ed, CRC Press, 2004, ISBN: 9780849304859.

[43] S Martoiu, H Muller and J Toledo, 'Front-end electronics for the Scalable Readout System of RD51', *IEEE NSS/MIC CR*, IEEE, 2011 2036–2038.

[44] M. Zamrowski, 'Entwicklung eines Datenerfassungssystems für die Auslese des TimePix-Chips', 2009.

[45] K Abe et al., 'The T2K experiment', *NIM-A* 659.1 (2011) 106–135.

[46] S. Biagi, 'Monte Carlo simulation of electron drift and diffusion in counting gases under the influence of electric and magnetic fields', *NIM-A* 421.1 (1999) 234–240.

[47] J. Kaminski, private communication, 2013.

[48] J. Abernathy et al., 'MarlinTPC: A common software framework for TPC development', *IEEE NSS/MIC CR*, IEEE, 2008 1704–1708.

[49] F. Gaede, 'Marlin and LCCD-Software tools for the ILC', *NIM-A* 559.1 (2006) 177–180.

[50] F. Gaede et al., 'LCIO-A persistency framework for linear collider simulation studies', *arXiv preprint physics/0306114* (2003).

[51] Research group of Taras Shevchenko, National University (Kyiv, Ukraine) in collaboration with LAL (Orsay, France) and IRFU (CEA, Saclay, France) research groups, private communication, 2013.

[52] C. Krieger, 'Construction and First Measurements of a GridPix based X-ray Detector', 2012.

[53] P. V. Hough, 'Method and means for recognizing complex patterns', tech. rep., 1962.

[54] R. Frühwirth et al., *Data analysis techniques for high-energy physics*, vol. 11, Cambridge University Press, 2000.

[55] S. Zimmermann, 'Data Reconstruction and Analysis of GEM-Based Time Projection Chambers with Pixel Readout', PhD thesis, diploma thesis at the University of Bonn, 2008.

[56] A. Sharma and R. Veenhof, 'Properties of some gas mixtures used in tracking detectors', *CERN. URL: http://consult. cern. ch/writeup/garfield/examples/gas/Welcome. html* (1998).

[57] R. Carnegie et al., 'Resolution studies of cosmic-ray tracks in a TPC with GEM readout', *NIM-A* 538.1 (2005) 372–383.

[58] J Beringer et al., 'Review of particle physics', *Physical Review D* 86.1 (2012).

# List of Figures

# List of Tables

# Acknowledgements

I would like to thank the workgroup of Prof. Klaus Desch in Bonn for their support and the most enjoyable atmosphere. I would also like to thank Hubert Blank, Walter Ockenfels and Dr. Rosenthal for their support during the design and assembly of the LP modules. Further, I would like to thank the testbeam team at DESY, which made the test of our modules possible.